

Peripheral Dipion Production by Pions of 12 and 18 GeV/c

LAWRENCE W. JONES,* E. BLEULER,† D. O. CALDWELL,‡ B. ELSNER,§ D. HARTING,||
W. C. MIDDELKOOP, AND B. ZACHAROV**
CERN, Geneva, Switzerland

(Received 27 June 1966; revised manuscript received 23 February 1967)

A spark-chamber experiment on the peripheral production of 9245 pion pairs by 12- and 18-GeV/c incident pions is reported and analyzed in terms of a one-pion-exchange model in which the final state at the nucleon vertex contains generally one or more pions. The relevant dynamics and kinematics appropriate to this problem are reviewed, and the experimental and analysis techniques giving good resolution and detection-bias correction are discussed in some detail. From the results, fair agreement is found between the data and the one-pion-exchange calculation of the ρ^0 production cross sections and of the associated missing-mass spectra. The ρ^0 is found to be consistent with a single peak, and no evidence of peak splitting is observed. A search for a narrow s -wave dipion resonance is made with negative results. Normalizing to the ρ^0 meson, the s -wave $\pi^+\pi^-$ scattering cross section is computed from the abundant low-dipion-mass events, giving a cross section falling smoothly from 50 mb (300 MeV) to about 20 mb (600 MeV). No evidence of an s -wave resonance is found in this range of energies. Below 450 MeV, the pion-pion scattering asymmetry favors backward scattering (by $2\frac{1}{2}$ standard deviations), which is consistent with a negative and falling $J=T=0$ phase shift. The extrapolated forward-backward asymmetry and the s -wave cross section are both consistent with a $J=T=0$ phase shift near $|90^\circ|$ at about 750 MeV.

I. INTRODUCTION

IN a CERN spark-chamber experiment designed to study peripheral production of pion pairs at high energies, 9245 interactions of 12- and 18-GeV/c negative pions with nucleons have been analyzed. The data were used to explore the character of the ρ^0 meson, peripheral ρ^0 "inelastic" production (i.e., ρ^0 accompanied by one or more pions at the nucleon vertex), the recoil mass spectra at the nucleon vertex in such production processes, and the $\pi^+\pi^-$ interaction in the s state. Because of the nature of the geometrical detection efficiencies, the data are most numerous for events of low momentum transfer and small dipion mass. The experimental technique required some novel features to achieve good resolution for the dipion system parameters at these high energies.

Results from a prototype experiment have been published,¹ and preliminary results from this experiment have been discussed as the analysis has progressed.²⁻⁵

* Present address: The University of Michigan, Ann Arbor, Mich. John S. Guggenheim fellow. Supported in part by the Ford Foundation and the U. S. Office of Naval Research, Contract No. Nonr 1224(23).

† John S. Guggenheim fellow. Present address: Pennsylvania State University, University Park, Pa.

‡ National Science Foundation senior fellow. Supported in part by the U. S. Atomic Energy Commission. Present address: University of California, Santa Barbara, Calif.

§ Present address: DESY, Hamburg, Germany.

|| Present address: Zeeman Laboratorium, Amsterdam, The Netherlands.

** Present address: Daresbury Nuclear Physics Laboratory, Daresbury, Lancaster, England.

¹ D. O. Caldwell *et al.*, Phys. Letters 2, 253 (1962).

² L. W. Jones, D. Harting, W. Middelkoop, B. Zacharov, D. O. Caldwell, E. Bleuler, and B. Elsner, The University of Michigan Technical Report No. 17 (unpublished); and Ya. A. Smorodinsky, in *Proceedings of the Twelfth Annual Conference on High-Energy Physics, Dubna, 1964* (Atomizdat, Moscow, 1965), p. 457.

³ L. W. Jones, Phys. Rev. Letters 14, 186 (1965).

⁴ L. W. Jones, E. Bleuler, D. O. Caldwell, B. Elsner, D. Harting,

In Sec. II the theoretical framework of the peripheral model as applied to this problem is reviewed and the special kinematical properties of high-energy "inelastic" production are presented. Section III presents details of the experimental design and performance, Sec. IV discusses the data-analysis procedures and in particular the detection efficiency problem, and Sec. V presents the normalization procedure. In Sec. VI the data are presented, and in Sec. VII observations are made on the character of the ρ^0 production cross-section magnitude, the missing-mass spectra, the s -wave pion-pion interaction, and the observation of more backward than forward pion-pion scattering at low dipion masses. A summary and acknowledgments complete the paper.

II. THEORY

A. Dynamics

The experimental data are all related to the general process in which a negative pion incident on a nucleon produces a pair of oppositely charged pions of rather high energy and an undetected recoiling nucleon or nucleon system. By restricting the events to small momentum transfers to the nucleon system and moderate values of the invariant mass at the nucleon vertex, we attempt to interpret the data in terms of a peripheral process involving one-pion exchange. The Feynman diagrams which will concern us are those of Fig. 1, where (a) represents the Chew-Low process of scattering of a real pion on a virtual exchanged pion, (b) is the same process except that a boson resonant state is assumed to be formed, and (c) and (d) correspond to (a) and (b) except that the final-state nucleon system is left excited

W. C. Middelkoop, C. R. Symons, and B. Zacharov, Nuovo Cimento 44A, 915 (1966).

⁵ L. W. Jones, D. O. Caldwell, B. Zacharov, D. Harting, E. Bleuler, W. C. Middelkoop, and B. Elsner, Phys. Letters 21, 590 (1966).

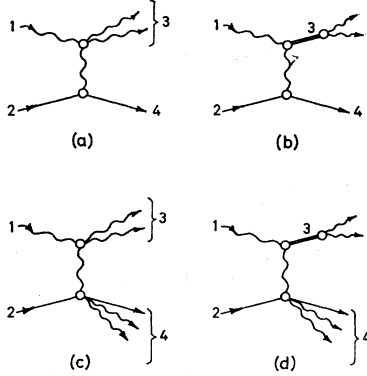


FIG. 1. Feynman diagrams appropriate for the peripheral reactions discussed here: (a) elastic meson scattering at the meson vertex, single nucleon recoil; (b) production of a meson resonance, single nucleon recoil (e.g., "elastic" ρ -meson production); (c) elastic meson scattering at meson vertex, recoil of an excited nucleon system; and (d) production of a meson resonance, recoil of an excited nucleon system (e.g., "inelastic" ρ -meson production).

to some higher energy and may decay through emission of pions. For convenience we shall refer to processes (a) and (b) as "elastic" and to processes (c) and (d) as "inelastic." We label the incident pion and nucleon as particles 1 and 2, respectively, and the emergent boson and nucleon systems as particles 3 and 4, respectively. The following definitions will be employed throughout:

- μ , the pion rest mass;
- m , the diboson rest mass (the invariant mass of particle 3);
- M , the nucleon rest mass;
- M' , the invariant mass of the outgoing nucleon system 4;
- t , the invariant four-momentum transfer carried by the exchanged particle (negative in the physical region), $t = (P_1 - P_3)^2 = -\Delta^2$;
- p , the momentum of the incident pion;
- q , the center-of-mass momentum of the "decay" pions of particle 3, $q^2 = (m/2)^2 - \mu^2$.

All energies and masses are expressed in GeV, and momenta in GeV/ c . In the expressions below we have put $\hbar = c = 1$.

In general, the cross section for Fig. 1 for one-pion exchange is given by⁶

$$\frac{d^3\sigma}{dm^2 dM'^2 d|t|} = \frac{1}{16\pi^3} \frac{m}{p^2 M^2} [\phi_{1,3}] \sigma_1(m) \frac{1}{(t - \mu^2)^2} M' [\phi_{2,4}] \sigma_2(M'), \quad (1)$$

where $\sigma_1(m)$ is the π - π interaction cross section at an

⁶ S. D. Drell, Phys. Rev. Letters **5**, 342 (1960); Rev. Mod. Phys. **33**, 458 (1961); F. Salzman, G. Salzman, Phys. Rev. **120**, 599 (1960). We would like to thank R. Deck, S. Drell, and B. E. Y. Svenson for clarifying the application of these expressions to our problem.

energy m ; $\sigma_2(M')$ is the π - N total cross section at an energy M' ; $[\phi_{1,3}]$ is the momentum of the incident pion in the center-of-mass (c.m.) system of particle 3; $[\phi_{2,4}]$ is the momentum of the target nucleon in the c.m. system of particle (system) 4:

$$\begin{aligned} [\phi_{1,3}] &= (1/2m) \{ [t - (m - \mu)^2] [t - (m + \mu)^2] \}^{1/2} \\ &= (1/2m) [(m^2 + \mu^2 - t)^2 - 4m^2\mu^2]^{1/2}, \\ [\phi_{2,4}] &= (1/2M') \{ [t - (M' - M)^2] [t - (M' + M)^2] \}^{1/2} \\ &= (1/2M') [(M'^2 + M^2 - t)^2 - 4M'^2 M^2]^{1/2}. \end{aligned}$$

For an s -wave π - π interaction characterized by a phase shift δ_0 in the rest frame of particle 3,

$$\frac{d^3\sigma}{dm^2 dM'^2 d|t|} = \frac{1}{8\pi^2} \frac{[2M' \phi_{2,4}] \sigma_2(M')}{p^2 M^2 (t - \mu^2)^2} \frac{m}{q} \sin^2 \delta_0 \quad (2)$$

if the isospin considerations are neglected. For the process $\pi^+\pi^- \rightarrow \pi^+\pi^-$ in an s state, both $T=0$ and $T=2$ phase shifts δ_0^0 and δ_0^2 can contribute, giving rise to a pion-pion scattering amplitude containing

$$\left(\frac{2}{3} e^{i\delta_0^0} \sin \delta_0^0 + \frac{1}{3} e^{i\delta_0^2} \sin \delta_0^2 \right). \quad (2')$$

For a p -wave π - π interaction, the spin of the outgoing dipion state adds off-mass-shell factors of $[\phi_{1,3}]$ to the expression, which gives, in terms of the p -wave phase shift δ_1^1 ,

$$\frac{d^3\sigma}{dm^2 dM'^2 d|t|} = \frac{1}{32\pi^2} \frac{[2M' \phi_{2,4}] \sigma_2(M') [2m \phi_{1,3}]^2 \sin^2 \delta_1^1}{p^2 M^2 (t - \mu^2)^2 m q^3}. \quad (3)$$

In the range of dipion masses considered here (below 900 MeV), the data from bubble chambers are consistent with the dominance of only three phase shifts, all real, in the pion-pion scattering: δ_0^0 , δ_0^2 , and δ_1^1 . Thus the scattering amplitude can be expressed more generally by

$$\left[\frac{2}{3} e^{i\delta_0^0} \sin \delta_0^0 + \frac{1}{3} e^{i\delta_0^2} \sin \delta_0^2 + 3(\phi_{1,3}/q) \cos \theta e^{i\delta_1^1} \sin \delta_1^1 \right],$$

where θ is defined as the polar angle between the incident and scattered negative pion in the dipion center-of-mass system. The corresponding azimuthal angle ϕ is equivalent to the Treiman-Yang angle and is defined as the angle between the dipion production and decay planes in the dipion c.m. system. A generalized expression for the differential cross section for the process of Fig. 1(c), which includes Eqs. (2) and (3) as special cases, can be written

$$\begin{aligned} \frac{d^4\sigma}{dm^2 dM'^2 d|t| d(\cos \theta)} &= \frac{1}{16\pi^2} \frac{[2M' \phi_{2,4}] \sigma_2(M')}{p^2 M^2 (t - \mu^2)^2} \left(\frac{m}{q} \right) \\ &\times \{ (4/9) \sin^2 \delta_0^0 + (4/9) \sin \delta_0^0 \sin \delta_0^2 \cos(\delta_0^0 - \delta_0^2) \\ &+ \frac{1}{3} \sin^2 \delta_0^2 + (\phi_{1,3}/q) \cos \theta [4 \cos(\delta_0^0 - \delta_1^1) \sin \delta_0^0 \sin \delta_1^1 \\ &+ 2 \cos(\delta_0^2 - \delta_1^1) \sin \delta_0^2 \sin \delta_1^1] \\ &+ 9(\phi_{1,3}/q)^2 \cos^2 \theta \sin^2 \delta_1^1 \}. \quad (3') \end{aligned}$$

If there is a resonance at energy m_0 (width Γ) in the ρ state, for example the ρ , the cross section is⁷

$$\frac{d^3\sigma}{dm^2 dM'^2 d|t|} = \frac{1}{16\pi^2} \frac{[2M'p_{2,4}]^2 \sigma_2(M') [2mp_{1,3}]^2}{p^2 M^2 (t - \mu^2)^2} \times \left(\frac{g^2}{4\pi} \right) \frac{m_0 \Gamma}{m^2 [(m^2 - m_0^2)^2 + (m_0 \Gamma)^2]}, \quad (4)$$

where $(g^2/4\pi)$ is the $\rho\pi\pi$ coupling constant, and moreover

$$m_0 \Gamma = \frac{2}{3} \left(\frac{g^2}{4\pi} \right) \frac{q^3}{m}$$

and

$$\sin^2 \delta = \frac{(m_0 \Gamma)^2}{(m^2 - m_0)^2 + (m_0 \Gamma)^2}.$$

The width Γ is a function of energy and for the ρ meson can be written

$$\Gamma = \Gamma_0 \left(\frac{q}{q_0} \right)^3 \left(\frac{m_0}{m} \right), \quad (4')$$

where q_0 and m_0 are the values of q and m at resonance. This energy dependence is of minor importance for the ρ case, and in general Γ will be set equal to Γ_0 . Numerically, for $m_0 = 750$ MeV,

$$(g^2/4\pi) = 0.02\Gamma \text{ (MeV)}.$$

For an integration over a range of dipion mass Δm centered at m_0 , Eq. (4) can be written as

$$\frac{d^2\sigma}{dM'^2 d|t|} = \frac{\chi}{16\pi} \left(\frac{g^2}{4\pi} \right) \frac{[2M'p_{2,4}]^2 \sigma_2(M') [2mp_{1,3}]^2}{p^2 m^2 M^2 (t - \mu^2)^2}, \quad (5)$$

where

$$\chi = (2/\pi) \tan^{-1}(\Delta m/\Gamma).$$

If particle 4 is a nucleon (i.e., $M' = m$), Eq. (5) becomes⁸

$$\frac{d\sigma}{d|t|} = \frac{\pi\chi}{4} \left(\frac{g^2}{4\pi} \right) \left(\frac{G^2}{4\pi} \right) \frac{(-t) [2mp_{1,3}]^2}{p^2 M^2 m^2 (t - \mu^2)^2}, \quad (6)$$

where $(G^2/4\pi)$ is the pion-nucleon coupling constant.

To Eqs. (2)–(6) multiplicative terms may be included to account for (i) vertex form factors, (ii) initial- and final-state interactions, and (iii) spin effects due to the spin of the final-state nucleon system M' . Since the target contains carbon, there could also be errors from the assumption that nucleons behave independently except for screening effects. On the other hand, the large values of M' which dominate our data would not be seriously suppressed by the Pauli principle, and we have no evidence of coherence effects since we find the dipion yield goes as $A^{0.61}$. Data at considerably lower energies have been brought into agreement with Eq. (6) by including somewhat arbitrary form-factor expres-

sions of the form⁸

$$F^2(t) = \left\{ \frac{0.72}{1 + [(\mu^2 - t)/4.73\mu^2]} + 0.28 \right\}^2. \quad (7)$$

Gottfried and Jackson have argued that a more reasonable physical basis for suppression of the cross section for the process of Eq. (6) at large values of $|t|$ is the interaction of the incident pion and outgoing particle, for example the ρ meson with the target nucleon at small impact parameters.⁹ It has been argued that much of this interaction might be included in an integration over final states at the nucleon vertex (integration over M'), as is done in the analysis below. Thus the small-impact-parameter, large-momentum-transfer initial- and final-state interactions at high energies may lead in most cases to excitation of the nucleon to isobar states without destroying the identity of the ρ or pion.³ On the other hand, form-factor effects should suppress the large-momentum-transfer interaction, independent of the M' integration.

Jackson has emphasized that the spin of the nucleon system may be taken into account by including terms $f(M')$ of the following form.⁷ If particle 4 is the $(\frac{3}{2})^+$ isobar ($M_0' = 1238$),

$$f_{(3/2)^+}(M') = \left[\frac{(M+M')^2 - t}{(M+M')^2 - \mu^2} \right]^2 \left[\frac{(M-M')^2 - t}{(M-M')^2 - \mu^2} \right]. \quad (8a)$$

If the particle 4 is the $(\frac{3}{2})^-$ isobar ($M_0' = 1512$),

$$f_{(3/2)^-}(M') = \left[\frac{(M+M')^2 - t}{(M+M')^2 - \mu^2} \right] \left[\frac{(M-M')^2 - t}{(M-M')^2 - \mu^2} \right]^2. \quad (8b)$$

If particle 4 is the $(\frac{5}{2})^-$ isobar ($M' = 1688$),

$$f_{(5/2)^-}(M') \cong \left[\frac{(M-M')^2 - t}{(M-M')^2 - \mu^2} \right]^3. \quad (8c)$$

In general, for angular momentum l ,

$$f_l(M') \cong \left[\frac{(M-M')^2 - t}{(M-M')^2 - \mu^2} \right]^l. \quad (8d)$$

Jackson further comments⁷ that it is not clear to what extent these factors should be retained when absorptive effects are important. Table I notes some numerical values for $f(M')$ for particular resonances. These correction factors would be upper limits at each value of M' and t , since the pion-nucleon resonances occur for the l values near $l_{\max} (\cong kR)$, and the important exponent in $f(M')$ is l_{\max} . Especially at larger M' , the different l values up to l_{\max} may give nearly equal contributions. The numerical cross sections calculated for the produc-

⁸ F. Selleri, Phys. Letters 3, 76 (1962).

⁹ J. D. Jackson, J. T. Donohue, K. Gottfried, R. Keyser, and B. E. Y. Svensson, Phys. Rev. 139, B428 (1965); J. D. Jackson, Rev. Mod. Phys. 37, 484 (1965).

⁷ J. D. Jackson, Nuovo Cimento 34, 1644 (1964).

TABLE I. Factors of $f(M')$ to be applied to Eqs. (2)–(5) to account for the spin of the final-state nucleon system M' .

$-t \sqrt{M'} \text{ (GeV)}$ $(\text{GeV}/c)^2 \sqrt{J^P}$	1.24 $(\frac{3}{2})^+$	1.51 $(\frac{3}{2})^-$	1.68 $(\frac{3}{2})^-$
0	1.28	1.14	1.12
0.05	2.06	1.52	1.45
0.10	2.87	1.98	1.85
0.15	3.70	2.44	2.32
0.20	4.55	3.08	2.85

tion of the ρ^0 by incident pions on nucleons are given in Table II for a variety of incident momenta.

According to the known properties of identified resonances, in addition to one-pion exchange the exchange of an A_2 meson could in principle contribute to the processes discussed in this paper. While no extensive calculations have been made, two observations are relevant. The spin of the A_2 would enhance its contribution relative to the pion: From the Regge-pole viewpoint, the A_2 trajectory crosses $t=0$ near $\alpha=0.5$, the pion trajectory crosses near $\alpha=0$, and the cross section should contain terms $s^{\alpha(t)}$ for each contributing trajectory. On the other hand, the propagator term $(t-\mu^2)^{-2}$ suppresses the cross section for exchanged particles of large mass μ , as almost μ^4 . The ratio of the propagator terms for A_2 and pion exchange is about 10^{-4} for $t=0$ and 240^{-1} for $t=-0.10$ $(\text{GeV}/c)^2$. The

magnitude of this suppression has encouraged us to ignore the possible contribution of A_2 exchange processes in this study.

B. Kinematics

This experiment differs from typical bubble-chamber experiments in at least two important respects: firstly, the incident pion energy was very high (12 and 18 GeV), and, secondly, the dipion data were analyzed by integrating over a range of M' at the nucleon vertex. These two factors resulted in some kinematical curiosities, noted below.

With p , m , μ , and M specified, the character of the outgoing system can be parametrized in different ways. The momentum of the boson in the laboratory p_3 and its lab angle with the incident pion θ_p were the measured variables. However, the choice of t and M' is equivalent to, and is more immediately related to, the physics. The choice of high incident energy and relatively small momentum transfers favors the selection of peripheral events, as does the restricting of the range of integration over M' . In Fig. 2, the available physical area in t , $(M')^2$ space is plotted for $m=750$ MeV and different values of p . The regions used in the analysis— $t < 0.3$ $(\text{GeV}/c)^2$, $M' < 2.5$ GeV, and $M' < 3.0$ GeV—are shown on an expanded scale in Fig. 3. That the reaction can still be quite peripheral despite a relatively large value of M' can be seen by computing $p-p_3$ as a function of M' and t . With $p \gg \mu, m$,

$$(p-p_3)^2 \cong \frac{M'^4}{4M^2} + M'^2 \frac{(M^2-t)}{2M^2} + \frac{(M^2-t)^2}{4M^2} - (M^2-t). \quad (9)$$

The dependence on t is small for $|t| < 0.3$ $(\text{GeV}/c)^2$ and $M' > 1.5$ GeV, and the relatively small value of $p-p_3$ for our range of M' can be seen in Fig. 4.

In spite of this favorable situation, the identification of an event with low $|t|$, $p_3 \cong p$, and $M' \cong M$ is still not necessarily a guarantee of a correctly labeled peripheral interaction. For example, the process $\pi^- + p \rightarrow \omega^0 + n$ can resemble the process $\pi^- + p \rightarrow (\pi^+ \pi^-) + N^*$ if the ω is produced with the minimum momentum transfer and the decay π^0 goes straight backward in the ω c.m. system. Numerically, an 18-GeV/c incident pion can make an ω of 17.8 GeV, which, if it decays as described above, can give two charged pions with a total momentum of 16.5 GeV/c and an effective invariant mass of 520 MeV, while the π^0 -neutron system will appear to have an invariant mass of only ~ 1.5 GeV. A similar misidentification would occur if an inelastically scattered pion produced an isobar which in turn decayed in such a way that a pion from the isobar, taken together with the fast, inelastic pion, appeared to constitute a dipion of invariant mass below 1 GeV. For example, an 18-GeV/c pion can inelastically scatter on a nucleon to produce a mass 1450-MeV isobar state, which can in turn decay into a pion and neutron such that the overall pion-pion-neutron final state is indistinguishable

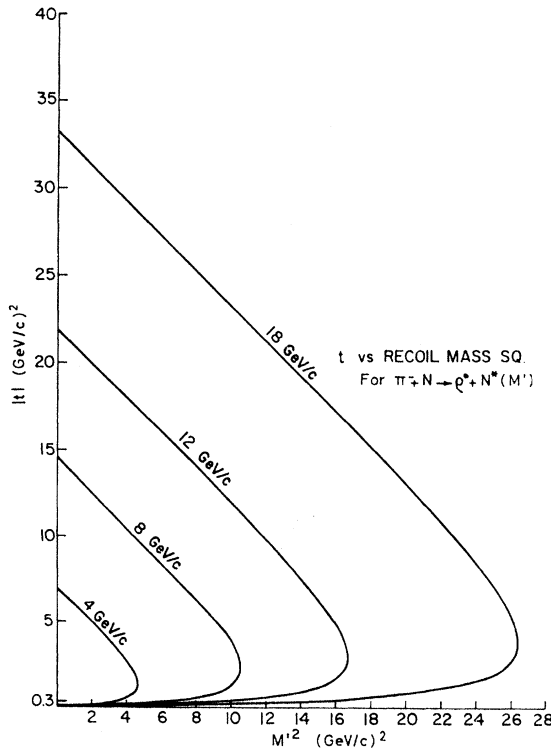


FIG. 2. The kinematic limits on missing mass M' versus four-momentum transfer t for the process $\pi^- N \rightarrow \rho^0 N^*$, where the state N^* has total energy M' . Curves for incident pion momenta of 4, 8, 12, and 18 GeV/c are presented.

TABLE II. One-pion-exchange calculation of elastic and inelastic ρ^0 production. The elastic cross sections are given with and without the Selleri form factor. The calculations used $\chi=1$, $m_0=750$ MeV, and $\Gamma_0=100$ MeV. The entries are cross sections in μb (10^{-30} cm^2).

$ t $ (GeV/c) ² \ p (GeV/c)		Elastic ρ^0 production cross section ^a [Eq. (6)]											
		4		8		12		18		50		200	
$ t $ (GeV/c) ²	p (GeV/c)	(a)	(b)	(a)	(b)	(a)	(b)	(a)	(b)	(a)	(b)	(a)	(b)
<0.05		213	124	53	31	24	13.8	10.5	6.1	1.36	0.80	0.085	0.050
0.05-0.10		192	78	48	19	21	8.7	9.5	3.8	1.23	0.50	0.077	0.031
0.10-0.20		303	87	76	22	34	9.7	15.0	4.3	1.94	0.56	0.121	0.035
0.20-0.30		261	56	65	14	29	6.2	12.9	2.8	1.67	0.36	0.104	0.022
<0.30		975	350	244	88	108	38.9	48.1	17.3	6.24	2.24	0.390	0.140
0.30-1.0		1766	245	441	61	196	27.2	87.2	12.1	11.30	1.57	0.706	0.098

$ t $ (GeV/c) ² \ p (GeV/c)		Inelastic ρ^0 production cross section [Eq. (5)]					
		4	8	12	18	50	200
<0.05			7.6		57		40
0.05-0.10			142		127		77
0.10-0.20			340		305		187
0.20-0.30			358		319		205
<0.30			848		809		509

^a Equation (6).

^b Equation (6) multiplied by $F^2(t)$ of Eq. (7).

from a $\rho^0 n$ state. Correspondingly, a collinear final state of $\pi^- \pi^+ n$ produced by a 12-GeV/c pion could be interpreted either as $\rho^0 n$ (with the ρ^0 produced at minimum $|t|$ and decaying with $\theta=0$) or as inelastic scattering to produce an isobar of mass 1320 MeV. However, in these two numerical examples the ambigu-

ous positive pion has a lab momentum of less than one GeV/c, while our system cuts off pions of less than three GeV/c, so that actual cases in our data of misidentification of pions from isobars should be very infrequent.

We believe that the vast majority of the events in our

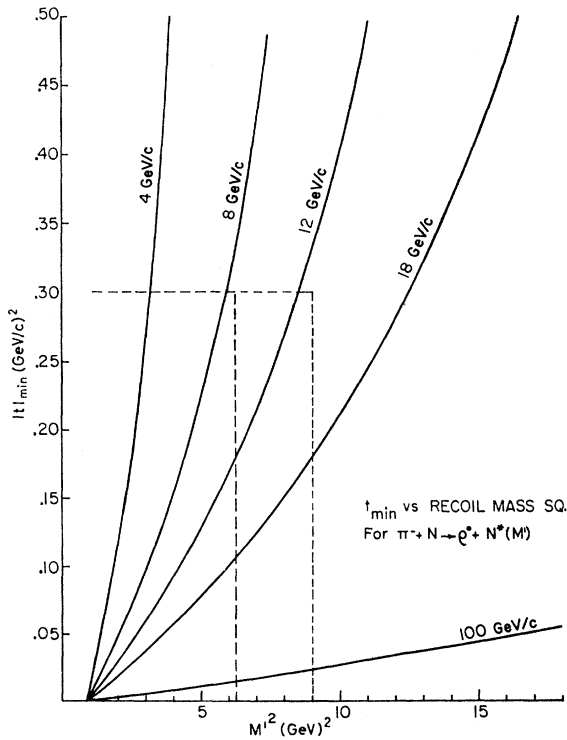


FIG. 3. The kinematic limits presented in Fig. 2 expanded for the region of M' , t of interest for this experiment. The limit for incident momentum of 100 GeV/c is also given in addition to those of 4-18 GeV/c. The regions used in the analysis are bounded by the dotted lines.

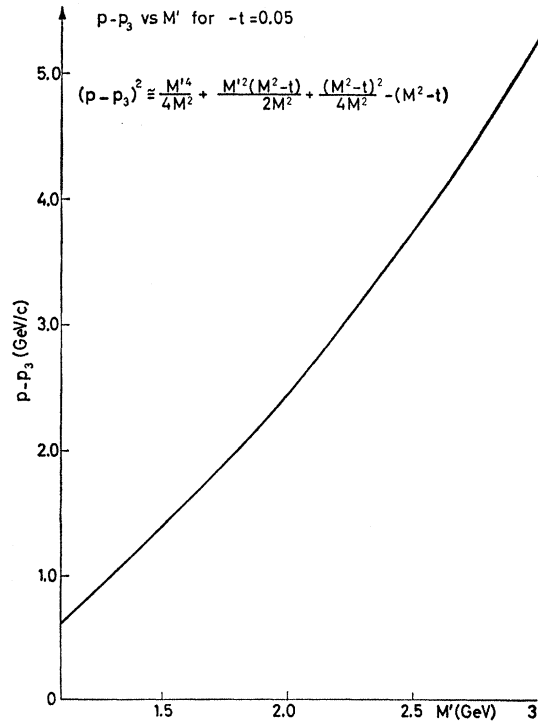


FIG. 4. The difference between incident pion momentum p and the outgoing dipion momentum p_3 , versus recoil nucleon mass M' for $-t=0.05$ (GeV/c)². The expression is approximately valid for $p \gg M'$, $p_3 \cong p$, and for dipion mass $m < M$, M' . The dependence on t is not strong, and the graph for $-t=0.20$ is very close to the curve given here.

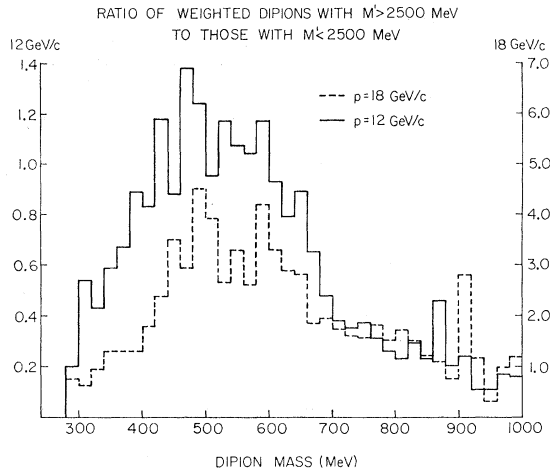


FIG. 5. The ratio of the weighted dipion events with $M' \geq 2500$ MeV to those with $M' < 2500$ MeV versus dipion mass m . The broad peak about 500 MeV is interpreted as due to the two charged pions from ω production.

analysis correspond, in fact, to the processes of Fig. 1 through the restrictions to small $|t|$, moderate M' , and $p_3 \simeq p$, since these cuts include a very small portion of the phase space for other channels. This situation is favored by our use of high energies, as the particle multiplicity increases as $E^{1/4}$, while the available phase space increases at least as E^2 and the populated perimeter of the phase plots increases as E^1 .

It is likely, on the other hand, that events with very large M' do contain many mislabeled events. Thus, a plot of events with $M' > 2.5$ GeV divided by events with $M' < 2.5$ GeV shows a broad peak near 500 MeV (Fig. 5), as one might expect from the distribution of the effective invariant mass of the two charged pion pairs from ω mesons. It is worth recalling that no amount of detailed kinematical data on any single event can determine to which vertex a particular pion should be associated, if both possibilities are kinematically

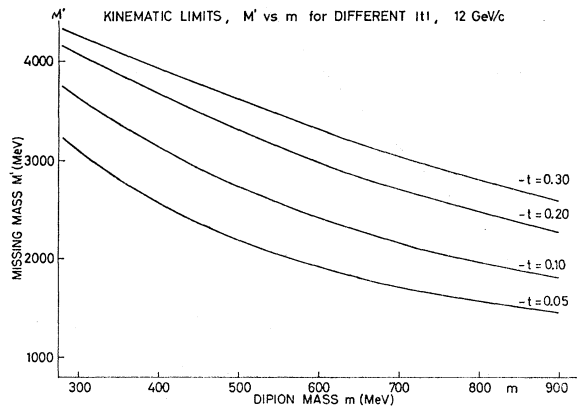


FIG. 6. The kinematic limits on missing mass M' versus dipion mass m for different values of four-momentum transfer t , and for 12 GeV/c incident momentum.

allowed, or indeed even whether a two-vertex peripheral diagram is appropriate.

The use of variables m , M' , and t for the final state complicates the analysis since the kinematical limit on M' , for example, depends on both m and t . In Figs. 6 and 7, the limiting curves of M' versus m are plotted for different values of t for p of 12 and 18 GeV/c. This is important in the evaluation of $d\sigma/dm$, as the factors in Eqs. (2)–(5) containing the M' dependence give a cross section which increases rapidly with the M' upper limit. Except for the factor $\sigma_2(M')$ (which varies slowly at larger M') the M' dependence of Eqs. (2)–(5) is of the form

$$d\sigma/dM' \propto M'[2M'p_{2,4}].$$

For the case of ρ -meson production, Eq. (5) can be simplified in the asymptotic limit of very high energy and small momentum transfer: $p \gg M' \gg M$, m ; $M > |t| > \mu$. With these limits the curves of Fig. 3 are

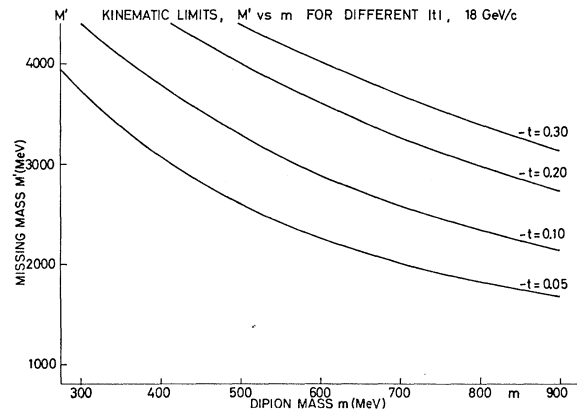


FIG. 7. The kinematic limits on missing mass M' versus dipion mass m for different values of four-momentum transfer t , and for 18-GeV/c incident momentum.

given approximately by

$$M'^2 \simeq -2Mpt/m^2 + M^2 \simeq -2Mpt/m^2.$$

Since $p_{2,4} \sim M'$ for $M'^2 \gg M^2$, $|t|$, the differential cross section for inelastic ρ^0 production can be approximated by

$$\frac{d\sigma}{d|t|} \propto \int_{(M')_{\min}}^{(M')_{\max}} \left(\frac{M'}{pt}\right)^2 dM'^2 \simeq \text{const.}$$

This result, independent of t and p , will lead to a violation of unitarity if extended to other boson resonance production and other exchange processes unless modifications of the theory are invoked to suppress the reaction at both larger momentum transfers and higher energies.

One significant feature of the high energy of this experiment is the long decay mean free path of emerging resonances, for example the ρ , relative to the range of

nuclear forces. If the ρ meson has a width $\Gamma = 100$ MeV, the decay mean free path is given numerically by $\lambda = 2\beta\gamma F$. Values of λ taken in the c.m. system of the final-state nucleon system M' are given in Table III for different incident momenta and for M' a single nucleon recoil ($M' = M$) or a recoiling system of $M' = 1.5$ GeV. The importance of a large λ in reducing distortions of a resonance has been discussed.¹⁰

In the study of the peak energy and width of a resonance such as the ρ , many factors enter which affect the interpretation. The m and q dependence of Γ would tend to lower the mass slightly (~ 5 MeV). On the other hand, the term $[2m\phi_{1,3}]^2$ weights the values towards larger mass (~ 5 – 10 MeV). However, for low $|t|$ the M' dependence on m and the strong weight of the maximum allowed M' on the cross section would lower the apparent peak energy in a manner depending on the t interval. Of course, physical effects resulting from the mixing of the two resonances in the nucleon force field¹⁰ may be a significant factor in shifting the ρ peak. Both the two-pion decay of the ω ¹¹ and the

TABLE III. Decay mean free path λ of a ρ meson ($\Gamma = 100$ MeV) in the recoil nucleon c.m. system for different incident pion momenta. The final state is considered a nucleon ($M' = M$) or a state of $M' = 1.5$ GeV.

p (GeV/c)	$M' = M$ λ (F)	$M' = 1.5$ GeV λ (F)
2	4.6	
4	9.9	
8	20.6	
12	31	18.6
18	47	29

$J = T = 0$ proposed ϵ meson^{12,13} could distort the data in the ρ -mass region, although neither would have a strong effect on the cross section integrated over the ρ peak.

III. EXPERIMENTAL ARRANGEMENT

In experiments above 10 GeV, the mass resolution attainable with spark chambers (outside a bending magnet) can be made comparable to or even better than that of other techniques. As momenta increase and angles decrease, good resolution can be maintained by increasing the spacing between components without significantly enlarging the detectors. Thus we believe

¹⁰ D. O. Caldwell and R. Weinstein, *Nuovo Cimento* **39**, 991 (1965).

¹¹ L. Durand and Y. T. Chiu, *Phys. Rev. Letters* **14**, 1039 (1965).

¹² L. Durand and Y. T. Chiu, *Phys. Rev. Letters* **14**, 329 (1965); M. Feldman, W. Frati, J. Halpern, A. Kanofsky, M. Nussbaum, R. Richert, P. Yamin, A. Choudry, S. Devins, J. Grunhaus, *ibid.* **14**, 869 (1965); and I. Derado, V. P. Kenney, J. A. Poirer, and W. D. Shephard, *ibid.* **14**, 872 (1965).

¹³ V. Hagopian, W. Selove, J. Aletti, J. P. Baton, M. Neveu-Rene, R. Gessarolli, and A. Romano, *Phys. Rev. Letters* **14**, 1077 (1965); A. H. Rosenfeld, in *Proceedings of the Oxford International Conference on Elementary Particles, 1965* (Rutherford High-Energy Laboratory, Chilton, Berkshire, England, 1966), Supplement, p. 5.

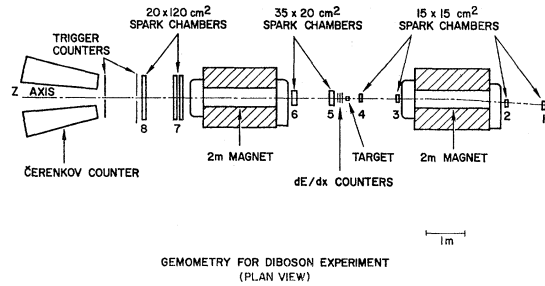


FIG. 8. A plan view of the geometry of the experiment, showing the relative locations of magnets, target, spark chambers, and counters. The spark chambers are numbered 1 through 8.

that this technique will become increasingly valuable and warrants detailed description here.

The apparatus, previously described briefly,¹⁴ consisted of two 2-m magnets and eight spark chambers, so designed that for each event the incoming pion and each of the two high-momentum outgoing bosons were momentum analyzed to about 1%. Čerenkov counters discriminated between outgoing pions and kaons over a portion of the solid angle, and an additional threshold Čerenkov counter in the beam permitted separation of incident pions and kaons. Data were taken under four sets of conditions with a target of polyethylene or of carbon and with the central momentum of the incident beam at 12.16 or 18.04 GeV/c.

A. Geometry

The apparatus is shown schematically in Fig. 8. Each of the spark chambers contained six 1-cm gaps and seven plates of 0.025-mm hardened aluminum foil, plus two 0.125-mm mylar windows. Chamber 7 (following the second magnet) was a double chamber. The chambers were constructed of Lucite rectangular frames cemented together and to the foils with epoxy.

The second, or analyzing, magnet had an aperture of 55×14 cm² and a pole length of 2 m. The front of the pole tips was 180 cm from the target so that the angle subtended by the magnet aperture from the target was 0.196 rad horizontally (to the center of the magnet) and 0.037 rad vertically (to the far end of the magnet). This small solid angle coupled with the long effective length of the magnet (2.05 m at 18 kG) biased strongly against detecting events other than those in which two high-momentum particles were produced at small angles. While this selection of peripheral events corresponded with the objectives of the experiment, it also necessitated a large bias correction for detected events. Thus, the probability of detecting a ρ meson produced with a small momentum transfer at 18 GeV was about 5%, and this detection probability was a function of all the kinematical variables characterizing the event. The

¹⁴ E. Bleuler, D. O. Caldwell, B. Elsner, D. Harting, L. W. Jones, W. C. Middelkopp, B. Zacharov, M. L. Perl, and C. C. Ting, *Nucl. Instr. Methods* **20**, 208 (1963).

manner in which this detection probability was evaluated and applied to the data is discussed below.

The spark chambers were arranged in pairs with the members of each pair spaced by 1 m, permitting a (nominal) 1-mrad angle measurement of each track entering or leaving a magnet. Fiducial marks on each chamber permitted the chambers to be carefully surveyed relative to the magnets and to each other.

B. Optics

The chambers and illuminated fiducial marks were photographed by a single camera at 55:1 demagnification onto 35-mm film with a 300-mm-focal-length lens. The image of each chamber was seen through three- or four-plane, front-surface mirrors. The optical system and its alignment were essentially the same as that used in an elastic scattering experiment and already described in detail.¹⁵

C. Trigger Logic

The purpose of the scintillation counters was to trigger the spark chambers and camera to record probable peripheral dipion events, which were those having one particle entering the target and two emerging in

through the solid angle and high field of the analyzing magnet. Behind the last spark chamber were two counters, one to the left of the symmetry axis ("z axis") of the apparatus and one to the right. These counters were slightly larger in area than the last spark chamber, and a coincidence between them was the main means of selecting a probable peripheral meson-production event. However, there is a first-order focusing of meson pairs of a given invariant mass m along the z axis of the system so that for a certain range of dipion masses the trigger efficiency would be very low with this arrangement. This problem was remedied by placing a second pair of coincidence counters about 1 m behind the first pair, as shown in Fig. 8, with the output of the two separate coincidences added in the trigger logic. The resulting trigger efficiency was a smoothly varying function of m , and fell off with increasing momentum transfer. The detection efficiency was very low when the pion pairs had the same charge or when the sign of their charges was such that they diverged in the magnet. In the analysis only oppositely charged pion pairs were considered.

In order to reduce spurious triggers from events produced by the beam beyond the target, a set of three 5-mm-thick scintillators was placed 20 cm beyond the target with the bias of each set at about $1\frac{1}{2}$ times the median pulse height for a minimum-ionizing particle. Thus a coincidence between all three indicated with a high probability that more than one particle had gone through the set; on the other hand, the probability that a dipion event from the target was missed in the counters was very small. The Landau pulse-height spread made the use of more than one counter essential. In practice, the bias on the counters was adjusted so that the loss of double-pion events was negligible, while the rate for spurious triggers was suppressed by about a factor of 10. Even with these counters, only about one event in ten was a dipion event useful for analysis. These dE/dx counters also provided a target themselves, constituting 40% as much material as was contained in the target, and 20% of the events were due to interactions in these counters. The z coordinates of the event vertices permitted the separation of events which came from the counters from those coming from the target, and the detection probability calculation took into account the proper event origin. Figure 9 contains a plot of vertex distributions in z for a sample of events.

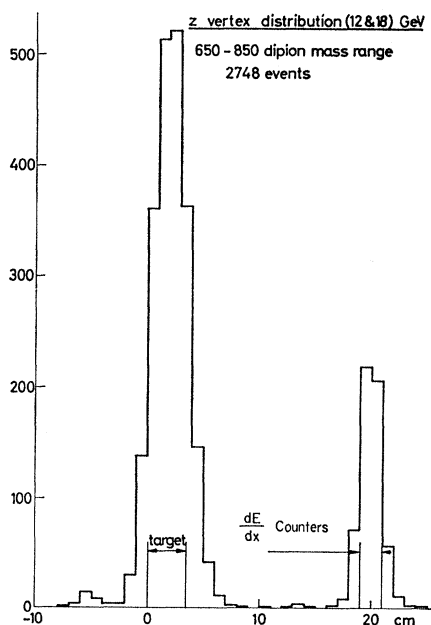


FIG. 9. The distribution in z of the vertices of ρ mesons produced by 12- and 18-GeV/ c incident pions. The geometrical extent of the target and the dE/dx scintillation counters is shown. There was an anticoincidence counter with an aperture for the incident beam a few centimeters to the left of the target.

¹⁵ D. Harting, P. Blackall, B. Elsner, A. C. Helmholtz, W. C. Middelkoop, B. Powell, B. Zacharov, P. Zanella, P. Dalpiaz, M. N. Focacci, S. Focardi, G. Giacomelli, L. Monari, J. A. Beaney, P. A. Donald, P. Mason, L. W. Jones, and D. O. Caldwell, *Nuovo Cimento* **38**, 60 (1965); D. Harting, thesis, University of Amsterdam, 1964 (unpublished).

D. Čerenkov Counters

Two large gas threshold Čerenkov counters were installed behind the last trigger counters to separate pions from kaons. Using gas (Freon-114 and Freon-22) at atmospheric pressure, the threshold for Čerenkov radiation could be set at $(1-\beta)=0.00137$ or $(1-\beta)=0.00075$, corresponding to separation of pions and kaons in the range either from 2.68 to 9.40 GeV/ c or from 3.62 to 12.8 GeV/ c . The counters were made of

THRESHOLD GAS ČERENKOV COUNTER

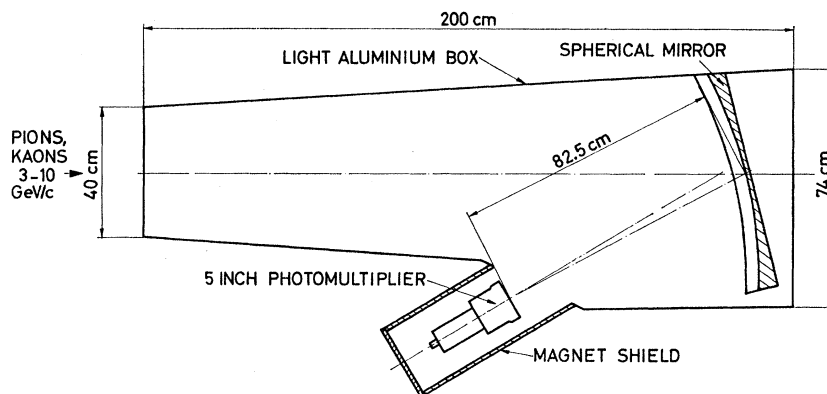


FIG. 10. Design of the gas threshold Čerenkov counters. The counters were always at the ambient atmospheric pressure, and operated with F-22 and F-114.

aluminum sheet metal, and each employed a single 5-in. photomultiplier (RCA 7046). A large spherical aluminum mirror collected the Čerenkov light onto the phototube. The counter design can be seen in Fig. 10. The Čerenkov counters were used to flash lights when they triggered in coincidence with an event trigger, and these lights were recorded on the film frame. The counters were tested in the pion beam and found to be 92% (one counter) and 96% (the other counter) efficient for pions along the axis. It is probable that a better figure for the average efficiency for pions through the counter in the experiment was closer to 90%. Of detected and analyzed events, 47% of the emerging bosons passed through a Čerenkov counter in the 12-GeV/c run and 44% in the 18-GeV/c run. Of the particles which passed through the counters, 26% did not trigger them in the 12-GeV/c run and 18% did not trigger them in the 18-GeV/c run. Allowing for an efficiency of about 90%, these data are consistent with emerging bosons consisting of 90% pions. In analyzing the data, we considered as dipions all events in which both of the bosons passing through a Čerenkov counter triggered it, and all events where the Čerenkov counter labeling did not exclude assignment as a dipion. The latter group included some kaon events from those in which the kaons did not pass through a Čerenkov counter and lacked some dipion events because of the inefficiency of the Čerenkov counter. The possible error in normalization from these sources is discussed in Sec. V.

E. Precision and Errors

The errors in determining momentum, dipion mass, missing mass, and other physical quantities came from the following: the alignment of the spark chambers and their fiducials in the laboratory, the alignment of the optics, the film resolution, the precision of film digitization, multiple Coulomb scattering, and magnetic field calibration. The original surveying precision was ± 0.2 – 0.3 mm in the laboratory. By autocollimation of the system the optics were aligned to correspond to a

maximum parallax error (between sparks and fiducial marks) of ± 0.3 mm, except in the horizontal views of the last large spark chambers (± 0.5 mm). The film was digitized to a precision of ± 7 - μ least count with image plane digitizers at CERN for approximately two-thirds of the events, and to ± 2.5 μ or ± 1 μ with focal-plane digitizers at Michigan and MIT for the remaining one-third of the events. The poorest figure corresponds to ± 0.4 mm in the laboratory and probably represents a working average uncertainty. Film grain did not seem to be a limitation here. These measurement errors combine to give ± 0.55 -mm uncertainty in the location of a track segment crossing a fiducial line. For two track segments spaced by 1 m, the corresponding angle uncertainty is ± 0.78 mrad. The error in determining a bending angle (momentum) or the opening angle of a pair of tracks is then ± 1.1 mrad. For a 2-m, 18-kG magnet, the bending angle-momentum product $p\theta = 1.08$ GeV/c rad. The momentum measurement uncertainty is then given by

$$\delta p = 0.92 p^2 \delta \theta = \pm 10^{-3} p^2; \quad \delta p/p = \pm 10^{-3} p. \quad (10)$$

For $p = 12$ GeV/c, $\delta p/p = \pm 1.2\%$; for $p = 18$ GeV/c, $\delta p/p = \pm 1.8\%$. These measurement errors constitute the main uncertainty at high momenta and are checked by comparing the momenta of beam pions as measured in the two magnets; such measurements bear out the validity of this analysis, giving $\pm 2\%$ as the measured difference between the momentum of 12-GeV/c beam pions between the two halves of the system and $\pm 3\%$ as the measured difference for 18-GeV/c beam pions.

While multiple Coulomb scattering adds to the momentum uncertainty, this additional error is compensated by the least-squares fitting to each track which is possible because of the overdetermination of the trajectory. The magnetic field calibration does not constitute an important error because the field is known from maps and from wire orbits to a precision of much better than 1%.

Multiple scattering can be important for low-momentum pions, however. It enters into (1) the

determination of the opening angle θ_0 of two emerging pions from the target and (2) the momentum of either pion. First, for the opening-angle determination, track coordinates in the two spark chambers beyond the target are read. Scattering in the target, the air, and the first spark chamber would affect this angle. Assuming that an average event originates in the target center, there are 0.08 radiation lengths of matter before the second spark chamber, corresponding to an angle uncertainty $\delta\theta = 0.0042/p$ (GeV/c). Thus, for a 4-GeV/c pion, multiple scattering would introduce an uncertainty comparable to the resolution factors discussed above. Second, the measurement of a momentum is deteriorated by multiple scattering in 5 m of air and two spark chambers containing 0.02 radiation lengths of material. This contributes an uncertainty $\delta\theta = 0.0021/p$ (GeV/c), so that the scattering uncertainty exceeds the measurement error only below 2.1 GeV/c, which is less than the momentum cutoff.

For momenta of the emergent pions, p_+ and p_- , large compared to the pion rest mass μ , and θ_0 small, the dipion mass is given by

$$m^2 = \mu^2 [2 + p_+/p_- + p_-/p_+] + p_+ p_- \theta_0^2.$$

For nearly symmetric decays, $p_+ \simeq p_-$,

$$\delta m \simeq \frac{1}{2} p_3 \delta\theta,$$

where p_3 is the dipion momentum in the laboratory. This expression includes the relationships of Eq. (10) above for this particular magnet, and the expression is valid to within a factor of two for p_+ and p_- differing by a factor of two. The discussion above leads us to expect errors in dipion mass of 1 or 2% even for ρ mesons produced at 18 GeV. From goodness-of-fit tests of measurements in the ρ -mass region, the errors in δm inferred from our data are ± 11 MeV (12-GeV/c ρ events) and ± 15 MeV (18-GeV/c ρ events), in substantial agreement with the expectation.

While the dominant dipion states studied here (e.g., the ρ^0) are too broad to permit a measurement of the

mass resolution, a qualitative check on the resolution is possible from a selection of $\pi^+\pi^-$ pairs from K_1^0 decays. Since the K_1^0 decay mean free path at these energies is tens of centimeters, a $K_1^0 \rightarrow 2\pi$ event should appear in our analysis as a dipion of mass 498 MeV with a "production" vertex downstream from the target. Accordingly, we have plotted (Fig. 11) the mass spectrum of dipions having the z coordinates of their vertices between 7 and 17 cm from the target center (e.g., between the target and the ionization counters). The background is due to poorly determined events from the target, and this background decreases with increasing opening angles, which occur for larger dipion masses and lower incident energy (i.e., 12 instead of 18 GeV/c). A clear peak can be seen in the 12-GeV/c data and an indication of a peak at 18 GeV/c. This meager K^0 data is consistent with or better than the resolution discussed above. The indication of a small mass shift is within the expected error in our absolute calibrations.

The missing mass M' is given approximately by

$$(M')^2 \simeq M^2 + 2M(p - p_3),$$

so that

$$\delta M' = (M/M')\delta(p - p_3).$$

For nearly symmetric dipion decays, $p_3 \simeq 2p^\pm$; the error δp^\pm should be about $\frac{1}{4}\delta p$, or δp_3 would be about $\sqrt{2}\delta p/4$. Hence the missing-mass error is dominated by the momentum error in the incident beam. From these considerations we believe that $\delta M' \simeq 0.17(M/M')$ for 12 GeV/c and $\delta M' \simeq 0.35(M/M')$ for 18 GeV/c. In addition to measurement uncertainties, the Fermi motion of nucleons in carbon adds further uncertainty in the missing mass, as the assumption that the target nucleon is initially at rest is not valid for those events not produced in the hydrogen of the CH_2 . If the Fermi momentum is p_3 , then the additional error in missing mass is roughly

$$\delta M' \approx -\mathbf{p}_2 \cdot (\mathbf{p} - \mathbf{p}_3)/M'.$$

This error is therefore greater the smaller M' and the larger the momentum transfer. In magnitude it is on the average approximately equivalent to the measurement error in M' given above.

The errors in the four-momentum transfer, dipion decay angles, etc., are all small and of less consequence in the analysis than are errors in dipion mass or missing mass.

IV. DATA ANALYSIS

A. Film Digitization

Over 200 000 photographs were taken in the experiment and scanned for probable diboson events. A typical film frame is shown in Fig. 12, and the spark-chamber positions on the film are given in Fig. 13. Selected frames of the film were digitized as described below. For each event the measurement consisted of recording coordinates of four fiducial marks and of two

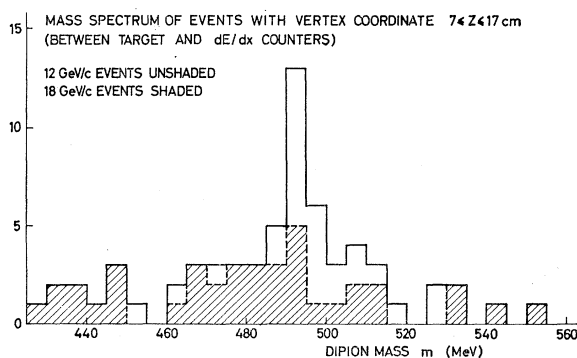


FIG. 11. The dipion mass spectrum of events with apparent vertices between the target and dE/dx counters showing a peak at the K^0 mass. This confirms the mass resolution and normalization as computed.

points for each track segment in each chamber. The points chosen to define the track segment were the intersections of a line superposed through the relevant set of six sparks and intersecting two parallel fiducial lines recorded on either side of each chamber view. The orientation of these reference lines was precisely known from surveying and from the measurement of a "fiducial set." A "fiducial set" was a digitization of 46 fiducial points on a film frame. These contained the four reference fiducials used for each event and from 2 to 6 fiducials for each of the 16 chamber views (two stereo views of each of the eight chambers). On the views of the larger chambers (35 and 120 cm), up to 6 fiducial measurements, or about one measurement every 15 cm of real space, permitted correction for distortion of the

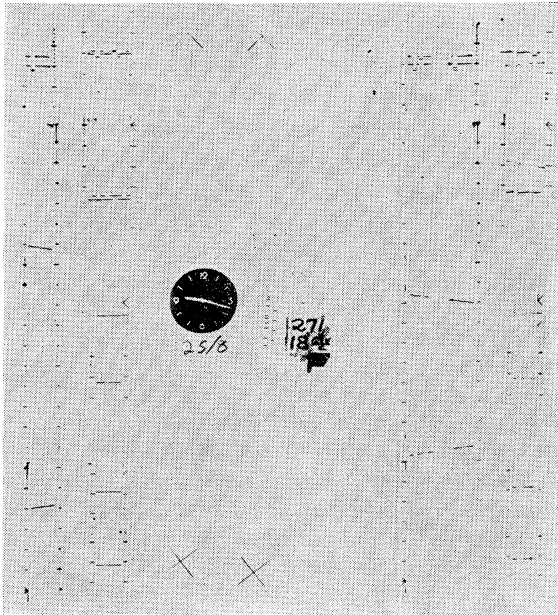


FIG. 12. A film frame of a typical dipion event. The spark chambers are bordered by fiducial lights.

image over the chamber area if there were curvature of the mirrors. These calibration measurements were stored in the form of geometrical transform coefficients in the computer. A "fiducial set" was measured about every 200 film frames and used as a reference for events recorded subsequently, since it was observed that gradual changes in mirror positions caused observable changes in the fiducial coordinates.

Each digitized event was stored on magnetic tape and processed by the SCRAP¹⁶ program system. There are four main phases of the SCRAP program: geometrical reconstruction, event selection on the basis of specified topology, geometrical optimization, and kinematic analysis. After geometrical reconstruction of each track

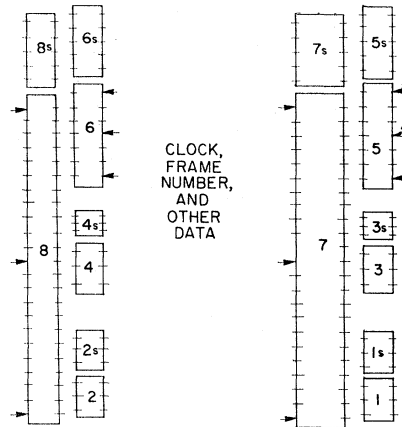


FIG. 13. A sketch of the film frame format showing the views of each spark chamber numbered as in Fig. 8. The lower member of each view pair is the direct (vertical) view; the upper member, specified *s*, is the stereo (horizontal) view.

in terms of real space parameters, the input data was filtered and selected for a possible two-prong event; in cases of ambiguity or of more than one interaction vertex, each possibility was stored sequentially for further processing. Thus, for example, frequently three or more closely spaced tracks appeared in the chambers just beyond the target, but only two tracks continued beyond the analysis magnet. In some of these cases the pairing of track segments to correspond to particle trajectories was ambiguous. Events not satisfying established criteria and tolerances were listed separately, together with the reason for their rejection.

Events which satisfactorily passed the selection phase of SCRAP were optimized by the use of constrained least-squares fitting techniques, which was possible here because the measurements overdetermined the topology. This feature was very valuable in obtaining the best values of spatial parameters and momentum for each track. In this experiment the optimization of the interaction vertex¹⁷ was performed separately from the trajectory optimization¹⁸ for each of the three relevant particles.

Because there was no kinematical overdetermination, analysis of each event was performed simply by calculating a suitable set of kinematic quantities completely specifying the event in both laboratory and c.m. systems. In general, since the nature of the decay particles could not be assumed *a priori*, the kinematical analysis was performed separately for three assumptions: both decay particles pions, both kaons, or one pion and one kaon. Then, with a knowledge of the momenta of the decay particles, their path length through the Čerenkov counters, and the threshold for detection in the counters together with the actual recorded response of the Čerenkov counters, a best

¹⁶ B. Zacharov (unpublished).

¹⁷ B. Zacharov, Nucl. Instr. Methods **32**, 163 (1965).

¹⁸ B. Zacharov, Nucl. Instr. Methods **33**, 136 (1965).

hypothesis could be made for the nature of the parent diboson (namely, dipion, dikaon, or kaon-pion).

All the parameters, both geometrical and kinematical, specifying each good event were stored on a data summary or abstract tape, together with the calculated errors and best kinematical hypothesis. The abstract tape was sorted, and duplicate events were eliminated and finally processed using the CERN SUMX routines in order to produce the histograms, lists, and other plots desired.

B. Weighting Factors

For each event two sets of detection probabilities (reciprocal weighting factors) were calculated and recorded on the abstract tape. For the first set (I), the diboson production azimuth was considered to be the only unessential variable, whereas all other variables—production coordinates, incident beam direction, dipion production, and decay polar angles, and relative decay azimuth—were kept as measured. The detection probability, then, was the range of production azimuthal angles which would allow the two particles to be detected, divided by 2π . For the second set (II), the decay probability was also assumed to be independent of the relative decay azimuth, as postulated by Yang and Treiman¹⁹ for a one-pion-exchange peripheral interaction.

Each of these two sets contains four different detection probabilities, depending on the possible use of the Čerenkov-counter information: (i) Neither of the particles was required to enter the Čerenkov counters. (ii) One particle had to traverse the left Čerenkov counter in such a manner that a pion could be distinguished from a kaon, whereas the other particle was not constrained. (iii) Same as (ii), but for the right-hand counter. (iv) Both particles had to be identifiable in their respective Čerenkov counters.

In each case, the azimuthal ranges were also constrained by the requirement of proper traversal through the scintillation coincidence counters; i.e., events triggered by a third particle would be discarded. Further restrictions arose from the requirements that both particles had to miss an anticoincidence counter placed immediately behind the magnet pole tips and that their lateral excursions in the magnet had to stay within limits set by the field dropoff. In setting these limits, we were forced by the complications arising from the field inhomogeneities to adopt arbitrary safe values and reject some events allowed by the coincidence and veto counters. In particular, the initial particle directions were required to lie between two planes defined by the production vertex and two lines 2 mm inside the horizontal boundaries of the window of the veto counter. Actually, the vertical focusing of the magnet's fringe field allows particles to pass the window even if they

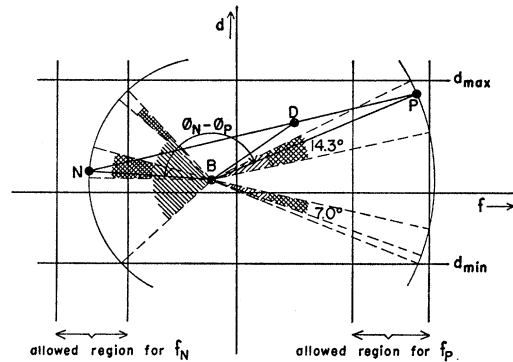


FIG. 14. Calculation of detection probability for fixed Treiman-Yang angle ϕ . The direction of each particle is represented by a point. B: beam particle, D: dipion, N: negative pion, P: positive pion. \parallel : allowed regions for P. \backslash : allowed region for N. Overlapping cross-hatching: allowed regions for both P and N, with fixed $\Delta\phi = \phi_N - \phi_P$. The detection probability given by the pair of allowed regions for f_P and f_N shown is $P_I = (14.3^\circ + 7.0^\circ)/180^\circ = 0.118$.

start with larger vertical excursions. Even though such events were detected, no detection probability was calculated for them, and they were not used for the computation of cross sections and angular distributions.

The method used for the calculation of a detection probability of set I is illustrated in Fig. 14. In this case $\Delta\phi = \phi_N - \phi_P$ is kept fixed, where the azimuthal ϕ angles are here measured in the laboratory and N and P refer to the negative and positive emergent pions, respectively. Note that fixed $\Delta\phi$ is equivalent to fixed ϕ , the Treiman-Yang angle defined in Sec. II. As shown in Fig. 14, the initial direction of each particle in the laboratory is represented by a point whose coordinates are $f \equiv dx/dz$ and $d \equiv dy/dz$. The limits d_{\max} and d_{\min} are set as described in the preceding paragraph. There are up to four pairs of allowed regions for the horizontal excursions, depending on the trigger and Čerenkov-counter requirements. They were obtained by using the main program to find, for selected values of f , the values of k (the central-field curvature of the path) which would make the particle hit the edges of the counters. Analytic approximations for the limits $f(k)$ for all counter edges were then found. The values $f(k)$ depend somewhat on d ; i.e., the vertical boundary lines in Fig. 14 should be slightly curved due to vertical focusing effects. Except for marginal cases, the influence of the curvature is small and has been neglected in this calculation. As shown in Fig. 14, the allowed azimuths for the two particles N and P (shaded regions) were calculated in the small-angle approximation, the loci for N and P being circles. Those parts of the allowed regions which overlap properly (cross-hatched), i.e., where $\phi_N - \phi_P$ has the fixed experimental value, yield the detection probability. Note that in the particular example of Fig. 14, P passes closer to the boundaries and hence determines more of the limiting angles than does N .

For set II, both the production and the decay

¹⁹ S. B. Treiman and C. N. Yang, Phys. Rev. Letters 8, 140 (1962).

azimuth were varied. Forty equal (9°) steps in the c.m. dipion decay azimuthal angle ϕ were taken. For each value of ϕ , an event with the same p , m , M' , t , ϕ , etc. was generated by the computer, and a detection probability of set I was computed. The ϕ -averaged detection probability P_{II} is then given by

$$P_{II} = \frac{1}{40} \sum_{i=1}^{40} P_{I_i},$$

where P_{I_i} are the appropriate set-I detection probabilities.

An alternative procedure for generating weighting factors would have been to make a Monte Carlo sample of events, compute their detection probabilities, and apply these to the observed events. However, such a procedure would be subject to bias unless an unreasonably large data sample was used. Each event is characterized not only by (p , m , M' , t , θ , and ϕ) but by the vertex coordinates in the target and the direction of the incident pion. In principle, the detection probability depends on all of these. As an example, in order to study ρ mesons produced at $|t| < 0.1$, $M' < 2500$ MeV, and $|\cos\phi| < 0.3$, some distribution of all variables would have to be assumed to choose the correct Monte Carlo sample. In the method used, the sample of events used to find such a detection probability is just the experimentally detected sample, so that the distribution of, for example, target vertices, is the most suitable one. This argument breaks down only where the detection probability as a function of some variable is zero over a fraction of the range of that variable considered. We have taken particular care to avoid this pitfall, and find that this is a serious problem here only for the ϕ decay angle of the dipion. For this reason we have computed and used the set-II weighting factors, where ϕ isotropy is assumed and the detection probability is computed accordingly.

V. NORMALIZATION

The data in this experiment are used in three ways: in raw form, weighted by the detection probability, and weighted and normalized for determination of absolute cross sections. The normalization was done separately for 12- and 18-GeV/ c incident pions and for carbon and polyethylene targets. Below, we discuss the parameters which enter into the normalizations and the resulting uncertainties.

In order to reduce the numbers of events to cross sections, it was necessary to know the ratio of events produced in the polyethylene target (with mass and momentum transfer cuts) to events produced in both the target and the dE/dx counter. This ratio was 0.769. With this correction it was no longer necessary to distinguish between events from the dE/dx counters and the target, except to use the correct vertex in the detection probability determination for each event.

About one-quarter of the film was carefully rescanned and remeasured to find the absolute number of detected and measured dibosons per incident beam pion. It was learned that a remaining 2% of the events may have been missed even on a second scan and second measurement. Another 3% were missed because program restrictions were placed on trajectories in the magnet and in defining a vertex in order to remove extremes of the distributions so as to reject spurious or false events.

A correction also had to be made for the composition of the incident beam. From measurements of beams of pions of this length and energy at CERN, it is known that there was a $(5 \pm 1)\%$ muon contamination in the pion beam. From 9245 events in the experiment, 60 were initiated by kaons, as deduced from a threshold Čerenkov counter in the incident beam.

The number of analyzed diboson events per incident beam particle was 2.794×10^{-5} based on 1819 dibosons from the 12-GeV/ c data and 1.247×10^{-4} based on 1143 dibosons from the 18-GeV/ c data. These figures include corrections for the fraction of the film from which good events were taken (e.g., no event was digitized from frames where two or more incident pions appeared in the spark chambers in front of the target). The entire data sample contains 5111 dibosons from the 12-GeV/ c data and 4134 dibosons from the 18-GeV/ c data. For a single event, the cross section is given by

$$\sigma_i = \frac{f}{\pi_0 n N E [\pi/(\pi+\mu)] P_i} \frac{1}{\text{cm}^2},$$

where f is the fraction of events from the target, 0.769;

π_0 is the number of incident mesons per event, corrected for the fraction of film used;

n is the total number of analyzed events;

N is the effective number of target nucleons per unit area, $0.885 \times 10^{24}/\text{cm}^2$ (see below);

E is the scanning and measuring efficiency, 0.95;

$[\pi/(\pi+\mu)]$ is the fraction of the beam which is pions, 0.95;

P_i is the detection probability of the event in question.

For the numbers presented above, the parameters give, for the two energies,

$$\sigma_i = 5.25 \times 10^{-33} (1/P_i) \text{ cm}^2 \text{ (12 GeV/c)},$$

$$\sigma_i = 2.89 \times 10^{-32} (1/P_i) \text{ cm}^2 \text{ (18 GeV/c)}.$$

The combined statistical uncertainties on these figures are $\pm 5\%$ due to statistics on all factors except N , the effective number of nucleons in the target.

Events contained in a certain interval of m , M' , t , $\cos\theta$, etc. are converted to a cross section by averaging their detection probabilities and multiplying the value of σ_i by the number of events. For example, if k events

have detection probabilities P_i ,

$$\bar{P} = \sum_{i=1}^k P_i/k;$$

$$\sigma = (5.25 \times 10^{-33} k/\bar{P}) \text{ cm}^2$$

if the events are from the 12-GeV/ c data.

In order to deduce an effective number of nucleons in the target (to infer a cross section per nucleon), data from the carbon and polyethylene targets were compared. This was done by comparing the ratios of events from each target to those from the dE/dx counters (sorted in the analysis according to the axial vertex coordinate of each event) at both energies. This method has the advantage of being independent of absolute normalization. The target events were used only for $M' < 2200$ MeV (12-GeV/ c data) or $M' < 2500$ MeV (18-GeV/ c data) and for $|t| < 0.30$ (GeV/ c)², while all analyzed events from the dE/dx counters were utilized. Table IV gives the numbers of events involved in this study, where the target events are further separated according to low- m events and ρ events. The carbon target consisted of a 2-cm, high-density carbon block fixed to a 5-mm-thick scintillation counter. It contained 5.67 g carbon, 0.04 g hydrogen. The polyethylene target was 3 cm CH₂ fixed to the same counter and contained 2.79 g carbon and 0.43 g hydrogen. The weighted average ratio of yields from the polyethylene and carbon targets was 0.670 ± 0.082 for $m < 650$ MeV events and 0.708 ± 0.097 for $650 < m < 850$ MeV (the ρ events). These values correspond to a dependence of the cross section on atomic weight as A^η , where $\eta = 0.56_{-0.16}^{+0.24}$ (for ρ events) and $\eta = 0.63_{-0.15}^{+0.25}$ (for $m < 650$). The large uncertainty is due to the small sample of data from the carbon target.

Since the difference between low-mass and ρ events is not significant, we have averaged the two ratios, giving a yield ratio of 0.687 ± 0.063 . The η value thus determined is $0.61_{-0.13}^{+0.14}$. The target contains then $1.47_{-0.26}^{+0.48}$ g of effective nucleons, or $0.885 \times 10^{24}_{-18\%}^{+33\%}$ effective nucleons. This error is reflected in an uncertainty in cross sections of -33% , $+18\%$. The difference in these numbers between 12 and 18 GeV/ c was not significant, and the data from the two

TABLE IV. Yield of dibosons from the target and from the dE/dx counters used to find the dependence of diboson yield on atomic weight for carbon. Events from the target are only those with $-t < 0.30$ (GeV/ c)² and $M' < 2200$ MeV (12 GeV/ c) or $M' < 2500$ MeV (18 GeV/ c).

ϕ (GeV/ c)	Target	Dibosons from dE/dx counters		Dibosons from target	
		$m < 650$ MeV	$650 < m < 850$ MeV	$m < 650$ MeV	$650 < m < 850$ MeV
18	CH ₂	544	589	358	
	C	97	144	93	
12	CH ₂	891	979	707	
	C	29	54	31	

energies are averaged above. The best value of the exponent, 0.61, would mean that the carbon nucleus contains 4.55 effective nucleons, or 2.27 protons and 2.27 neutrons. Thus, for the polyethylene target approximately two-thirds of the effective nucleons are protons, half of them bound in carbon, and one-third of the nucleons are neutrons, all bound in carbon. For comparison with theory we shall consider the proton-neutron ratio in the target as 2:1.

As discussed above in connection with the Čerenkov counters, the labeling of events as dipions is subject to uncertainty both because only about half the bosons

TABLE V. Relevant percentages of bosons which passed through the Čerenkov counters, and the indicated fraction which were kaons.

ϕ (GeV/ c)	Neither boson through a counter	One of two bosons through a counter	Both bosons through both counters
	12	24.3%	57.5%
18	35.8%	39.9%	24.3%
12 and 18	29.4%	49.6%	21.0%

ϕ (GeV/ c)	Counter No. 1	Counter No. 2	Average of No. 1 and No. 2	% labeled as kaons
	12	69.6%	79.6%	74.2%
18	85.6%	78.0%	81.9%	18.1%
12 and 18	76.2%	79.0%	77.5%	22.5%

ϕ (GeV/ c)	Dipions	Dikaons and kaon-pion pairs
	12	52.9%
18	72.3%	27.7%
12 and 18	63.0%	37.0%

ϕ (GeV/ c)	One boson labeled; kaons missed	Neither boson labeled; dikaons and kaon-pions missed	Total over- estimate of dipions
	12	57.5% \times 0.258 = 14.8%	24.3% \times 0.471 = 11.5%
18	39.9% \times 0.181 = 7.2%	35.8% \times 0.277 = 9.9%	17.1%
12 and 18	49.6% \times 0.225 = 11.2%	29.4% \times 0.370 = 10.9%	22.1%

ϕ (GeV/ c)	Percentage of all events not labeled as probable dipions.	
	12	17.5%
18	12.5%	
12 and 18	15.3%	

pass through Čerenkov counters and because the efficiency of the counters is not precisely known. Table V lists relevant percentages of bosons which passed through the Čerenkov counters and the indicated fraction which were kaons. From these figures, maximum errors on dipion yields can be obtained under one of two extreme assumptions: either the Čerenkov counters are 100% efficient and the number of kaons is relatively large, or the lack of a count in the Čerenkov counter indicates only inefficiency, and every boson is a pion. In the first case, if one assumes that each boson missing a counter is as likely to be a kaon as those detected, then the overestimate on dipion cross sections by

assuming that all bosons which missed the counters were pions is 26% (12 GeV/c), 17% (18 GeV/c), or 22% for the weighted average over 12 and 18 GeV/c. This is an extreme limit, as we know that Čerenkov counters are not 100% efficient; a suitable standard deviation would be about half of these figures. In the second case, if all dibosons are dipions the cross section has been underestimated by 18% (12 GeV/c), 13% (18 GeV/c), or 15% for the weighted mean of 12 and 18 GeV/c. Again these are extreme limits to the error. If the appropriate standard deviations are half of these figures, then for the combined data the Čerenkov counters

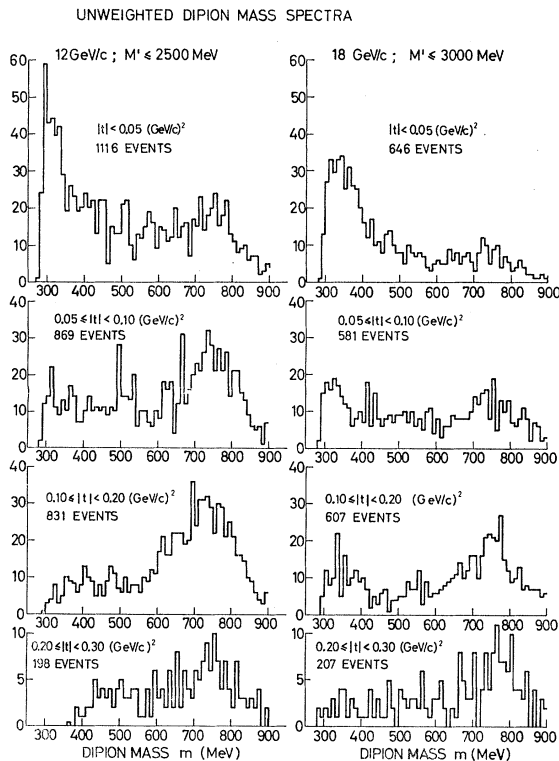


FIG. 15. Unweighted dipion mass spectra for 12- and 18-GeV/c incident momenta in the four different intervals of four-momentum transfer t . The ordinates are numbers of events in each 10-MeV dipion mass interval. Missing-mass cuts have been imposed as indicated.

introduce an uncertainty in the dipion normalization, and consequently in the cross sections, of +8%, -11%. Combining this with the statistical uncertainty ($\pm 5\%$) and the A^{η} uncertainty, +18%, -33%, the over-all normalization of the data is uncertain by +20%, -38%.

VI. DATA

A. Unweighted Dipion Spectra

The raw dipion mass spectrum data are given in Figs. 15-17. These histograms are presented mainly to show the number of events in different regions of mass

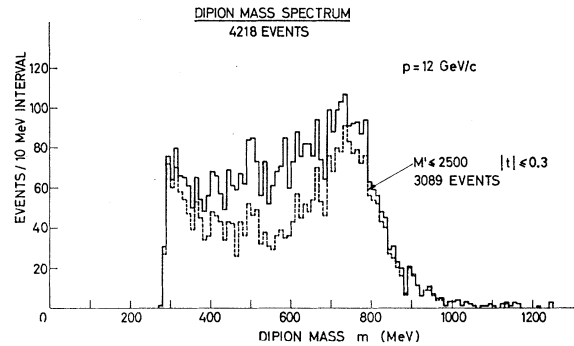


FIG. 16. Unweighted dipion mass spectrum as in Fig. 16 with all 12-GeV/c data taken together. Also shown is the 12-GeV/c mass spectrum of all events without restriction in missing mass or momentum transfer.

and momentum transfer. While the ρ^0 meson can be located, the main trends in the spectra are a consequence of the known but varying detection probability. In particular, the peak at low m (and especially at low t) is due entirely to the large detection probability.

It has been suggested¹³ that a narrow peak in the $\pi^+\pi^-$ s -wave system could be seen in the presence of a large ρ by selecting only events with small $|\cos\theta|$. On this basis the Pennsylvania group reported a peak between 700 and 750 MeV. We have selected all events in our unweighted data between 600 and 900 MeV with $|t| < 0.10$ (GeV/c)² and $|\cos\theta| < 0.30$. This mass spectrum is plotted in Fig. 18. For comparison, the data in the same dipion mass interval but without cuts in t or $\cos\theta$ are given in Fig. 19. The slowly falling detection probability is apparent, and there is some evidence of a broadly peaked resonance roughly corresponding to the ρ even in Fig. 18. However, we do not see any peak which would have a width narrower than 100 MeV and a mass less than 750 MeV. As this data sample contains over three times more events than the published Pennsylvania data, we believe that their evidence may have been only a statistical fluctuation.

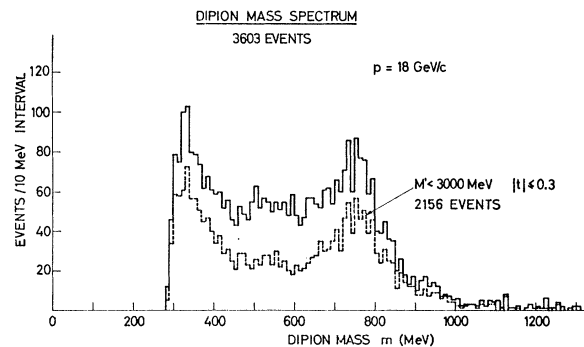


FIG. 17. Unweighted dipion mass spectrum as in Fig. 16 with all 18-GeV/c data taken together. Also shown is the 18-GeV/c mass spectrum of all events without restriction in missing mass or momentum transfer.

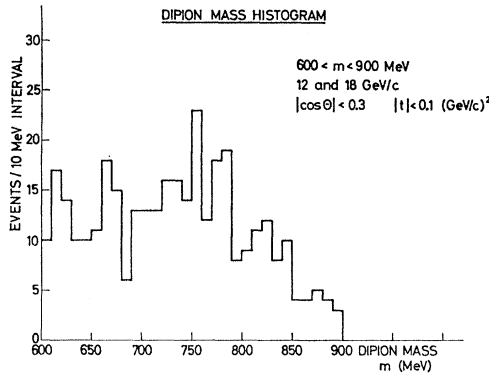


FIG. 18. Unweighted dipion mass spectrum for those events between 600 and 900 MeV, $|\cos\theta| < 0.3$, and four-momentum transfer $|t| < 0.1$ (GeV/c)². This selection was made to seek evidence of an *s*-wave dipion resonance in the presence of the dominant ρ^0 .

B. Weighted Data

As discussed in Sec. IV, a detection probability P_{II} was assigned to each event. All data were divided into the two incident momentum groups, p of 12 and 18 GeV/c; four intervals of momentum transfer $|t|$, with cuts at 0.05, 0.10, 0.20, and 0.30 (GeV/c)²; 25-MeV bins of dipion mass m ; and bins of 0.10 in $\cos\theta$. For a given interval of m , p , and t , the dependence of detection probability on M' was found to be less than 12% over the ranges considered, and consequently no dependence of the detection probability on M' was used.

For each interval of p , t , m , and $|\cos\theta|$ an averaged detection probability was found on all events within the interval. Then for each p and t interval, a two-dimensional smoothing was performed on the averaged

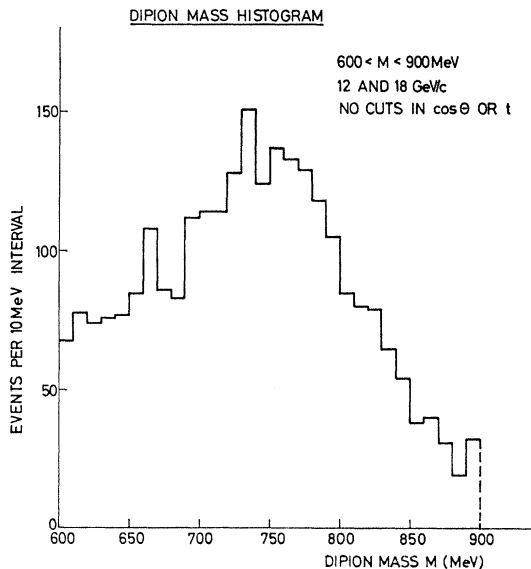


FIG. 19. Unweighted dipion mass spectrum for all events between 600 and 900 MeV with no restriction on $\cos\theta$ or t other than $|t| < 0.3$ (GeV/c)² and limits on missing mass M' as in Fig. 15.

detection probabilities versus m and $|\cos\theta|$. This removed anomalies due to statistical fluctuations in detection probabilities within each interval (seldom over about 20%). It was necessary to take care that weighted distributions were taken only over intervals wherein P_{II} is nonzero; when the detection probability falls to zero within an interval, the number of weighted events is an underestimate by an unknown amount. Therefore, in fits discussed below, a cutoff was made at the $|\cos\theta|$ interval next lower than the highest one containing events. Similarly, to avoid these zeros the

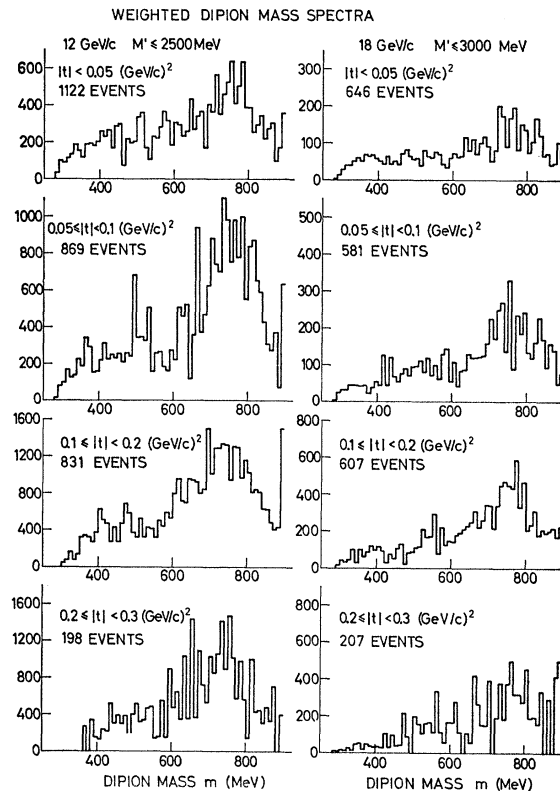


FIG. 20. Dipion mass spectra of Fig. 15 weighted according to the average detection probability as a function of dipion mass in each momentum transfer interval. No account was taken here of the dependence of detection probability on $\cos\theta$, nor of the varying $\cos\theta$ distributions with dipion mass. The ordinate scale is in arbitrary units.

detection probabilities were computed averaging over the ϕ angle of the pion-pion system, as has been discussed in IV. We, therefore, have in our results no test of the Treiman-Yang isotropy.¹⁹ In specific cases we have compared our observed ϕ distributions with the distribution obtained from a Monte Carlo sample of ϕ -isotropic events sent through the same geometry. From these tests we can say that our data are consistent with ϕ isotropy. The ϕ distribution found in lower-energy bubble-chamber data is sufficiently isotropic so that our $\cos\theta$ and mass plots would not be altered by the amounts of anisotropy reported.

Dividing the number of events in each interval by the average smoothed detection probability for that interval then gave a number of weighted events which could be interpreted directly as a cross section, as discussed in Sec. V.

The weighted data were sufficiently sparse when subdivided as described above that fits in 25-MeV intervals of dipion mass to $\cos\theta$ expansions were not very significant. Therefore, two separate treatments of the data were made. First, the weighted data were summed over all observed values of $\cos\theta$ for each 25-MeV dipion mass interval in each of the p and t intervals. This gave a mass spectrum of dipions in each interval of momentum transfer. When in turn these distributions were summed over all observed momentum transfers, a mass spectrum was obtained for each value of p which could reveal any fine structure in the mass distribution. However, the resulting mass spectra were not unbiased, because the true dipion distributions may vary with $\cos\theta$. For instance, in the ρ mass region where large $|\cos\theta|$ values are favored in the production but inefficiently detected, these mass plots underestimate such mass values relative to the low-mass region of the spectrum. These results are plotted in Figs. 20 and 21.

Using the data weighted in this way, we investigated the mass and width of the ρ^0 meson peak, in particular studying any possible splitting of the peak into two subpeaks or any systematic shift of the peak position with momentum transfer. Data from 600–900 MeV in dipion mass were fitted in each momentum transfer interval.

The results of this fitting are given in Table VI. In no case did the fit to a two-peak hypothesis show a better χ^2 than did the one-peak fit, and we conclude that in this data there is no evidence of a split peak. There is some trend toward a larger value of m_0 with larger $|t|$, although this may not be significant. The width Γ is less significant in this data, as it will be influenced by the changing angular distributions through the resonance region and the varying detection probability with θ , the pion-pion polar scattering angle. In particular, the detection probability is greater for smaller values of $|\cos\theta|$, and the ρ meson contributes mostly large $|\cos\theta|$. This can result in an erroneously large Γ for the ρ and we believe that the values of Γ are therefore overestimates of the true widths of the ρ meson. On the other hand, fits to the data after extrapolating the $\cos\theta$ distributions would suffer in statistical significance from the various uncertainties in these manipulations.

The second treatment of the data combined the weighted numbers of events over 100-MeV dipion mass intervals but different $\cos\theta$ intervals. These weighted data were then fitted to a $\cos\theta$ expansion:

$$f(\theta) = a_0 + a_1 \cos\theta + a_2 \cos^2\theta,$$

and the value $b_0 = a_0 + a_2/3$, which is related to the total

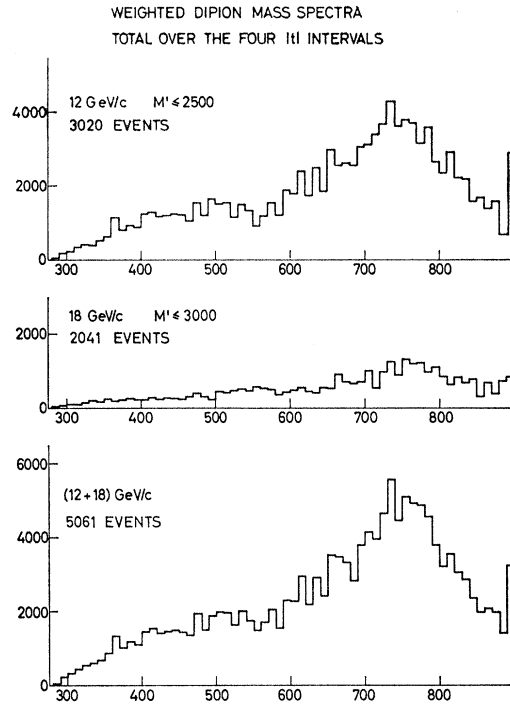


FIG. 21. The dipion mass spectra of Fig. 20 summed over the four intervals of momentum transfer for each incident momentum separately and together. Combining the data from 12 and 18 GeV/c involves a rather arbitrary relative normalization. The ordinate scale is in arbitrary units. The abscissa is dipion mass m (MeV).

cross section, was obtained. The fitting program also gave errors in these four coefficients. By the relationship given in Sec. V, these coefficients were reduced to absolute cross sections. Tables VII and VIII give values of a_0 , a_1 , a_2 , and b_0 with errors for each 100-MeV interval of dipion mass over the ranges of t covered. Also given are the values in μb of σ , the dipion production cross section, in each interval.

It is possible to improve the data presentation by combining the 25-MeV-interval mass spectra obtained ignoring the angular dependence with the 100-MeV-interval mass spectra deduced from the $\cos\theta$ fits. We

TABLE VI. Breit-Wigner resonance fits to dipions in range $600 < m < 900$ MeV. Fit made to the weighted data using a Breit-Wigner resonance plus a linearly varying background.

	$ t $ range (GeV/c) ²	m_0 (MeV)	Γ_0 (MeV)	χ^2 per degree of freedom
$p = 12$ GeV/c ^a $M' < 2500$ MeV	<0.05	765 ± 6	129 ± 19	1.30
	0.10–0.20	749 ± 5	157 ± 16	0.58
	0.20–0.30	750 ± 8	102 ± 25	0.94
$p = 18$ GeV/c $M' < 3000$ MeV	<0.05	745 ± 13	169 ± 41	0.68
	0.05–0.10	760 ± 9	175 ± 30	1.25
	0.10–0.20	761 ± 6	157 ± 19	0.63
	0.20–0.30	780 ± 10	157 ± 31	0.72

^a Because of a computer error, the values for 12 GeV/c, $0.05 < |t| < 0.10$ (GeV/c)², were lost

TABLE VII. Fits of the weighted 12-GeV/ c data, in 100-MeV dipion mass intervals, to $f(\theta) = a_0 + a_1 \cos\theta + a_2 \cos^2\theta$; $b_0 = a_0 + \frac{1}{3}a_2$. The cross section in each interval is found from b_0 and the normalization of Sec. V. The errors are statistical only.

Four-momentum transfer $ t $ (GeV/ c) ²	Dipion mass (MeV)	a_0	a_1	a_2	b_0	σ (μb)
<0.05	300-400	57 ± 10	-24 ± 15	49 ± 28	73 ± 7	7.73 ± 0.83
	400-500	99 ± 16	-6 ± 23	-8 ± 43	96 ± 12	10.2 ± 1.3
	500-600	66 ± 14	45 ± 27	74 ± 46	91 ± 13	9.5 ± 1.4
	600-700	108 ± 20	-15 ± 35	2 ± 67	109 ± 17	11.5 ± 1.8
	700-800	122 ± 31	296 ± 85	672 ± 184	347 ± 51	36.4 ± 5.4
	800-900	35 ± 19	237 ± 102	811 ± 561	306 ± 176	32.1 ± 18.5
	0.05-0.10	300-400	-17 ± 15	-7 ± 16	134 ± 39	27 ± 7
400-500		52 ± 22	-30 ± 26	100 ± 53	86 ± 14	9.1 ± 1.5
500-600		41 ± 16	34 ± 35	212 ± 65	112 ± 18	11.8 ± 1.9
600-700		74 ± 23	196 ± 45	273 ± 90	165 ± 24	17.4 ± 2.5
700-800		203 ± 42	351 ± 117	797 ± 242	469 ± 69	49.3 ± 7.3
800-900		40 ± 21	207 ± 135	1401 ± 477	508 ± 151	53.3 ± 15.9
0.10-0.20		300-400	-18 ± 47	0.9 ± 19	150 ± 74	31 ± 24
	400-500	468 ± 533	-17 ± 59	-227 ± 634	392 ± 324	41.2 ± 34.1
	500-600	415 ± 243	19 ± 66	-202 ± 332	347 ± 137	36.5 ± 14.4
	600-700	126 ± 32	372 ± 98	904 ± 165	428 ± 52	45.0 ± 5.5
	700-800	132 ± 46	410 ± 164	2320 ± 429	905 ± 125	95.1 ± 13.2
	800-900	137 ± 48	123 ± 211	685 ± 821	365 ± 246	38.4 ± 25.8

assumed that no rapid changes in the angular distributions occurred within intervals of less than 100 MeV; then the structure of the mass spectrum within each 100-MeV interval was determined from the 25-MeV spectra, but the normalization over each interval was taken from the accurately extrapolated coefficients of the $\cos\theta$ distributions using 100-MeV intervals. The resulting mass spectra are given in Figs. 22 and 23. Even in these plots the ρ meson appears less strongly

than lower dipion masses when compared with low-energy bubble-chamber data. This follows because the data here are integrated over M' , and more M' "space" is included in the low- $(-t)$, low- m data than in the ρ data for the same t . As the raw data is manipulated as described here, some errors in detail are bound to creep in. For example, the statistics of the $800 < m < 900$ MeV data at 12 GeV/ c are quite poor, but to the extent that they exist they fit a large a_2/a_0 (small Q value in Table

TABLE VIII. Fits of the weighted 18-GeV/ c data, in 100-MeV dipion mass intervals, to $f(\theta) = a_0 + a_1 \cos\theta + a_2 \cos^2\theta$; $b_0 = a_0 + \frac{1}{3}a_2$. The cross section in each interval is found from b_0 and the normalization of Sec. V. The errors are statistical only.

Four-momentum transfer $-t$ (GeV/ c) ²	Dipion mass (MeV)	a_0	a_1	a_2	b_0	σ (μb)
0.05	300-400	21.3 ± 3.0	-1.7 ± 5.9	9.2 ± 11.5	24.4 ± 3.1	14.1 ± 1.7
	400-500	21.5 ± 4.6	6.1 ± 9.0	10.5 ± 16.9	25.1 ± 4.5	14.5 ± 2.6
	500-600	11.0 ± 4.5	12.2 ± 10.3	50.7 ± 24.8	27.9 ± 6.4	16.1 ± 3.7
	600-700	16.0 ± 5.1	37.6 ± 15.9	80.8 ± 31.0	42.9 ± 8.9	24.8 ± 5.1
	700-800	17.7 ± 7.0	69.0 ± 23.6	159.8 ± 46.3	71.0 ± 14.4	41.0 ± 8.3
	800-900
	0.05-0.10	300-400	7.9 ± 2.3	4.2 ± 4.7	17.6 ± 7.4	13.8 ± 2.2
400-500		15.3 ± 6.1	8.2 ± 9.0	34.8 ± 18.5	26.9 ± 4.6	15.5 ± 2.6
500-600		24.0 ± 7.0	13.6 ± 12.7	30.8 ± 21.9	34.2 ± 6.4	19.8 ± 3.7
600-700		21.8 ± 7.7	-0.7 ± 17.9	72.1 ± 30.4	45.9 ± 8.9	26.5 ± 5.1
700-800		44.7 ± 11.7	87.9 ± 32.6	203.2 ± 61.5	112.5 ± 18.3	65.0 ± 10.6
800-900		26.4 ± 11.7	4.7 ± 23.7	77.4 ± 48.6	52.2 ± 12.1	30.1 ± 7.0
0.10-0.20		300-400	54.6 ± 17.7	-6.9 ± 7.4	-42.8 ± 25.2	40.3 ± 10.0
	400-500	32.5 ± 31.6	11.8 ± 9.0	-9.7 ± 46.2	29.3 ± 17.0	16.9 ± 9.8
	500-600	27.9 ± 16.1	0.6 ± 12.8	13.3 ± 31.5	32.4 ± 9.0	18.7 ± 5.3
	600-700	39.0 ± 14.6	79.3 ± 24.9	119.2 ± 40.8	78.8 ± 13.2	45.5 ± 7.6
	700-800	35.5 ± 14.7	99.5 ± 40.5	489.5 ± 83.6	198.6 ± 23.8	114.8 ± 13.7
	800-900	31.4 ± 15.5	47.3 ± 29.3	154.2 ± 70.8	82.8 ± 17.3	47.8 ± 10.1
	0.20-0.30	300-400	21.0 ± 10.1	-1.6 ± 5.5	-13.6 ± 15.1	16.4 ± 5.8
400-500		171.6 ± 90.8	6.8 ± 16.8	-179.3 ± 115.2	111.8 ± 53.1	64.6 ± 30.7
500-600		41.8 ± 75.3	5.5 ± 16.9	128.3 ± 104.8	1.0 ± 41.4	0.6 ± 24.0
600-700		0.6 ± 72.4	5.0 ± 24.2	111.9 ± 103.0	37.9 ± 40.5	21.9 ± 23.4
700-800		-10.1 ± 67.9	65.2 ± 30.7	231.9 ± 115.1	67.2 ± 34.3	38.8 ± 19.8
800-900		46.7 ± 16.9	-58.5 ± 36.7	65.3 ± 49.6	68.4 ± 18.4	39.5 ± 10.6

XI). This forces an extrapolation of the data to larger cross section values near 800 MeV and shifts the apparent ρ^0 peak energy to higher masses than the corresponding 18-GeV/c data. We do not believe that this represents any genuine discrepancy between 12 and 18 GeV/c, or with data from lower energies. It does indicate some of the potential pitfalls in this procedure, and it is for this reason that the most significant interpretations of the data are those after a minimum of manipulations. The data on the ρ -meson peak mass and width cited above were thus taken with only the first weighting procedure applied to the data.

VII. RESULTS

From the weighted dipion spectra and angular distributions, several physics analyses can be made. Over the 100-MeV interval from 700 to 800 MeV, the ρ^0 production cross section can be found as a function of t and p . From the isotropic portion of the data, a production cross section for s -wave dipions can be obtained and an s -wave pion-pion cross section deduced. The ratio of s to p wave can be found, and the forward-backward asymmetry versus dipion mass and momentum transfer can be determined. Finally, missing-mass spectra for low dipion mass and for ρ mesons can be analyzed.

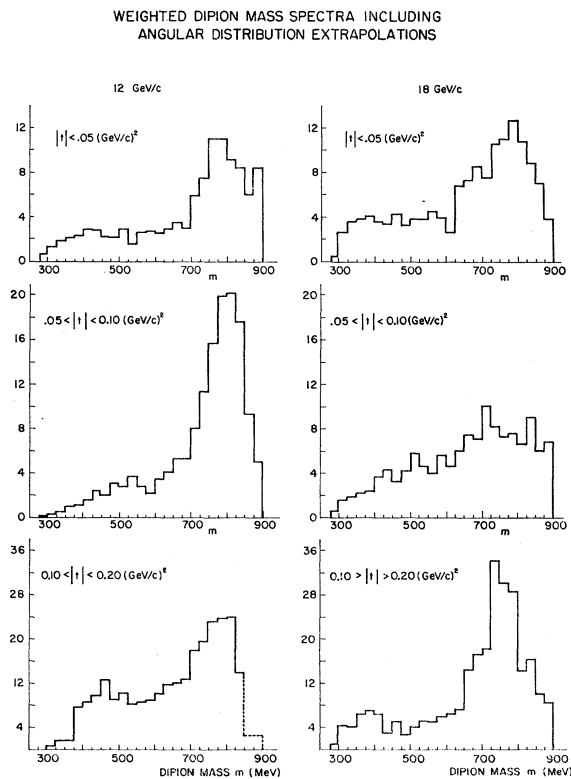


FIG. 22. Dipion mass spectra of Figs. 15 and 20 weighted including effects of the $\cos\theta$ detection probability. The actual weighting procedure is described in the text. The ordinate scale is in arbitrary units.

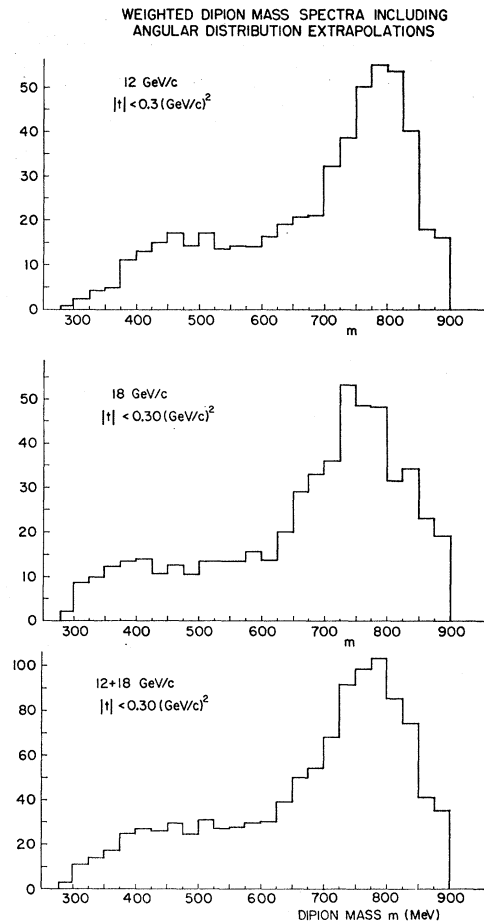


FIG. 23. The dipion mass spectra of Fig. 22 summed over the four intervals of momentum transfer for each incident momentum separately and together. Combining the data from 12 and 18 GeV/c involves a rather arbitrary relative normalization. The ordinate scale is in arbitrary units. These histograms differ from Fig. 21 in that the $\cos\theta$ dependence of detection probability and dipion production has been included.

A. Production of the ρ^0 Meson

The values of b_0 for $700 < m < 800$ MeV as discussed above were converted to cross sections, and these dipion production cross sections are given in Table IX for p of 12 and 18 MeV/c and in each interval of t . Also given are the values calculated from Eq. (5), where the calculation has used $m_0 = 750$ MeV, $\Gamma = 100$ MeV. The calculation contains the terms $\chi(g^2/4\pi)$, which reduce to $(0.04/\pi) \Gamma \arctan(\Delta m/\Gamma)$; thus for $\Delta m \approx \Gamma$ the calculated cross section depends only weakly on the value of Γ assumed. Table X gives the calculated and observed ratios of "elastic" ρ production (i.e., production of a ρ^0 and an unexcited recoil nucleon) to "inelastic" ρ production (where one or more pions are produced at the nucleon vertex). It is evident that elastic production is unimportant compared to the inelastic channels, except in the lowest momentum transfer interval.

As can be seen in Tables IX and X, the ρ production

TABLE IX. Comparison between normalized experimental cross sections for inelastic ρ^0 production and the one-pion-exchange calculation of Eq. (5) over the dipion mass interval $700 \leq m < 800$ MeV. For the calculation, the ρ^0 is characterized by $m_\rho = 750$ MeV, $\Gamma = 100$ MeV.

	Four-momentum transfer $-t$ (GeV/c) ²	$\sigma_{(\mu b)}$ calculation Eq. (5)	$\sigma_{(\mu b)}$ ^a experiment	$\sigma_{(\mu b)}$ ^b experiment corrected for elastic production
$p = 12$ GeV/c, $M' < 2500$ MeV	< 0.05	42	36.4 ± 5.4	30
	$0.05-0.10$	89	49.3 ± 7.3	47
	$0.10-0.20$	201	95.1 ± 13.2	94
$p = 18$ GeV/c, $M' < 3000$ MeV	< 0.05	42	41.1 ± 8.3	36
	$0.05-0.10$	89	65.1 ± 10.6	64
	$0.10-0.20$	184	114.8 ± 13.7	114
	$0.20-0.30$	131	38.8 ± 19.8	39

^a The values are from Tables VII and VIII. The errors are statistical. There is an additional normalization uncertainty of +20%, -38%.

^b The ratio of elastic to inelastic ρ^0 production as deduced from the missing mass spectra as given in Table X was used to correct the experimental values as given in the last column.

data agree well with the calculation at low $-t$ but fall below the unmodified calculation for larger $-t$ as expected from form factors or absorption effects.²⁰ This

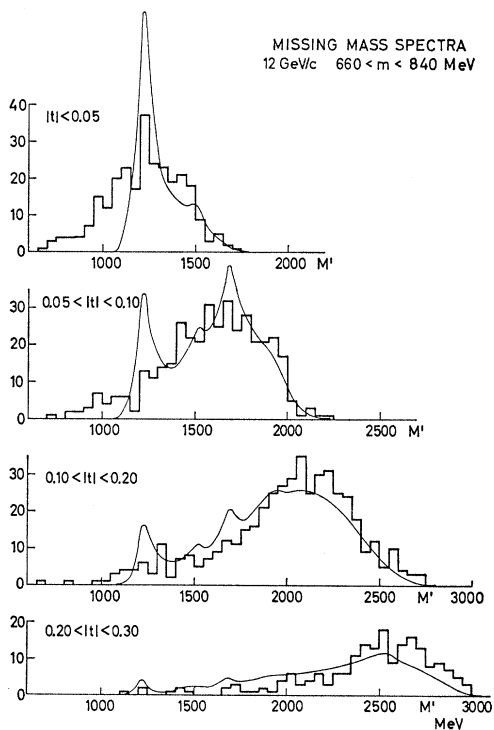


FIG. 24. The experimental distributions of missing mass M' for ρ^0 production by 12-GeV/c incident pions. The data are divided into the intervals of four-momentum transfer of Fig. 15. The calculated spectra, normalized in area to the events with $M' > 1050$ MeV, are superimposed as smooth curves. This data sample contains 1319 events. The ordinates are numbers of events in each 50-MeV interval of M' .

²⁰ These results differ, especially for larger $-t$, from the preliminary results reported earlier (Refs. 2 and 3) for three reasons: first, the number of events was doubled over the earlier data

departure is reduced when only the "inelastic" ρ production events are considered. As noted in Sec. II, off-mass-shell terms would modify the calculation, but not in a manner which varies strongly with t . While the observed dipion angular distribution in this mass region is only $\sim \frac{2}{3} \cos^2\theta$, the depolarization of ρ mesons due to absorption effects would give a departure from pure $\cos^2\theta$, and we interpret the data as consistent with ρ production dominating this mass region. There is, however, no quantitative formulation of the absorption model for inelastic ρ production as studied here. Nevertheless, the rather large value of the a_2 term (i.e., $\cos^2\theta$) in this mass region is further evidence that our data, suitably restricted in t and M' , are freer of background than are data taken at lower energies, in conformity with the arguments of Sec. II.

In a heavy-liquid bubble-chamber experiment exposed to negative pions of comparable energy, a relatively large A_1 meson production was reported and has been interpreted as resulting from a predominantly

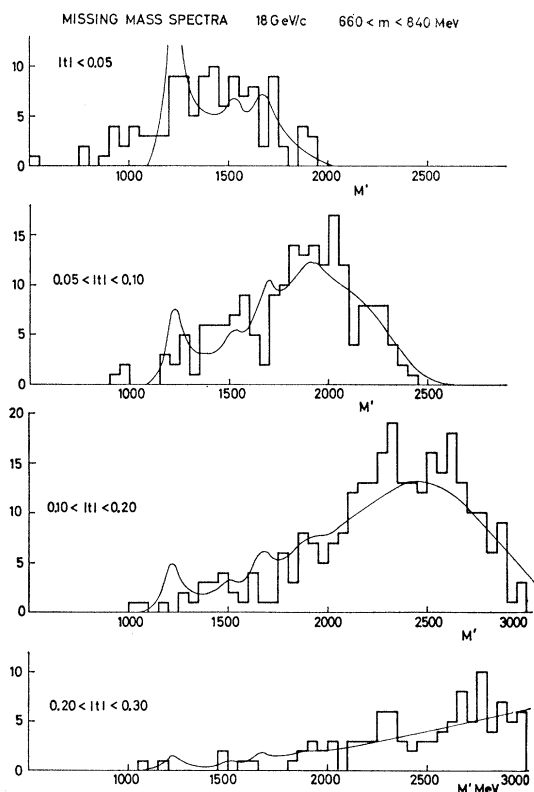


FIG. 25. The experimental distributions of missing mass M' for ρ^0 production by 18-GeV/c incident pions. The data are divided into the intervals of four-momentum transfer of Fig. 15. The calculated spectra, normalized in area to the events with $M' > 1050$ MeV, are superimposed as smooth curves. This data sample contains 693 events. The ordinates are numbers of events in each 50-MeV interval of M' .

sample; second, the fitting and weighting procedures were considerably refined; and third, an error in the calculation of the angle variables in the dipion c.m. system was located and corrected.

TABLE X. Comparison of elastic to inelastic ρ^0 production. Define elastic ρ production as that where a single neutron recoils, $M' < 1050$ MeV; inelastic ρ production as that where an excited nucleon system, $M' > 1050$ recoils. The calculation compares the elastic cross sections with a form factor applied [columns (b), Table II] to the inelastic cross sections with no form factor. $M'_{\max} = 2500$ MeV (12-GeV/ c data) and 3000 MeV (18-GeV/ c data).

Incident pion momentum p (GeV/ c)	Four-momentum transfer $-t$ (GeV/ c) ²	Elastic events observed	Inelastic events observed	Elastic to inelastic ratio observed	Elastic to inelastic ratio calculated (from Table II)*
		N_e 500 < $M' < 1050$ MeV	N_I 1050 < $M' < M'_{\max}$	N_e/N_I	N_e/N_I
12	<0.05	50	222	0.225	0.159
	0.05-0.10	19	368	0.052	0.048
	0.10-0.20	4	459	0.009	0.023
	0.20-0.30	1	195	0.005	0.014
18	<0.05	14	101	0.139	0.072
	0.05-0.10	3	188	0.016	0.022
	0.10-0.20	1	279	0.004	0.011
	0.20-0.30	0	103	...	0.007

* The theoretical ratios are $\frac{1}{3}$ the ratios of the cross sections of Table II as the target contains only $\frac{1}{3}$ (effective) protons.

coherent peripheral process.²¹ In our method of analysis, most of the ρ mesons from A_1 meson decay would have a momentum too low (e.g., corresponding to too large an apparent M' and $-t$) to be included in our data sample. Correspondingly, it is probable that relatively few of our events would appear as only three-prong events in a bubble chamber, considering the large M' values typifying our data. Therefore, we suspect that our results and theirs are mutually compatible, and that the total ρ meson production may in fact be close to the sum of the two processes.

B. Missing-Mass Spectra from ρ^0 Production

In Figs. 24 and 25 the missing-mass spectra are plotted together with theoretically computed curves. The curves are normalized to the data for $M' > 1050$ MeV. Much of this data has been discussed previously,⁴ so we note here only the important results. The experimental resolution on missing mass is poor, not even clearly separating the free nucleon recoils from N^* recoils. In spite of this, the trend suggests that the inelastic ρ production falls less rapidly than the elastic ρ production with momentum transfer. It also appears from the graphs that the lower isobars, particularly the $N^*(1238)$, are less prominent than the unmodified calculation would suggest. Off-mass-shell factors (Table I) would somewhat increase the $N^*(1238)$ contribution relative to higher isobars. However, the combination of poor missing-mass resolution and the effects of Fermi momentum can probably explain the washing out of this and other peaks.

From the values in Table I and the M' spectra of Figs. 24 and 25, it is apparent that at larger $-t$ values the larger M' values are the major contributors to ρ

production. Thus the entries of Table I which appear along a diagonal are the largest contributors to the cross section, and therefore if these off-mass-shell factors are indeed necessary they should give close to a factor of 2 correction to the calculated cross sections over this range of t .

The rate of fall of $d\sigma/dt$ and the increase of M' with $-t$, together with the ρ production magnitudes discussed above, lend support to the idea that absorption processes at the nucleon vertex may lead to more highly excited isobar (or simply inelastic) pion-nucleon states (larger M') without necessarily subtracting from the ρ production integrated over the inelastic channels. To be sure, absorption processes at the meson vertex may still attenuate ρ production with increasing momentum transfer, and form-factor effects may also play a role.

C. $\pi^+\pi^-$ Interaction in the s -Wave State

In Table XI and Fig. 26, we present the ratio of the isotropic to the total dipion production, a_0/b_0 of Tables VII and VIII. This ratio Q shows a consistent decrease from threshold to beyond the ρ mass. The values of a_0 from Tables VII and VIII taken together with the weighted dipion mass spectra in 25-MeV intervals of Fig. 22 can be used to find the cross section for producing dipions in an s wave. From Eq. (2), a corresponding theoretical calculation is available for the same process based on the same assumptions as the ρ calculation of Eq. (4). The calculated s -wave cross section, modified by the ratio of the measured to calculated ρ production (to take roughly into account absorption, form-factor, and off-mass-shell effects), could then be compared with the data to deduce a $\pi^+\pi^-$ cross section in the s wave. Since the forward-backward asymmetry suggested that δ_0^0 was close to $(\pi/2)$ for $700 < m < 800$ MeV (see below), the total $\pi\pi$ cross section in this range would be only about 27/31 due to the ρ^0 , and this ratio was also included in the normalization. Assuming that the $J=0$,

²¹ J. F. Allurd, D. Drijard, J. Hennessy, R. Huson, A. Lloret, J. Six, J. J. Veillet, G. Bellini, M. DiCorato, E. Firoini, P. Negri, M. Rollier, J. Crossard, J. Ginestet, A. H. Tran, H. H. Bingham, R. Diebold, W. B. Fretter, H. J. Lubatti, W. Michael, and K. Moriyasu, Phys. Letters 19, 431 (1965).

RATIO OF ISOTROPIC TO TOTAL PION-PION SCATTERING, Q , VS
MOMENTUM TRANSFER, t , FOR DIFFERENT DIPION MASS INTERVALS

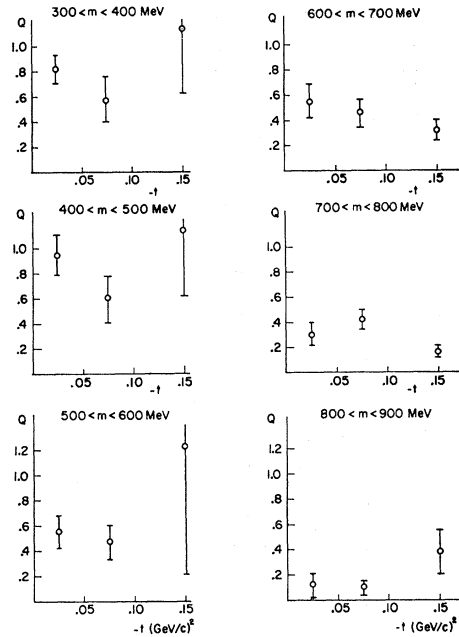


FIG. 26. The ratio Q of the production of isotropically-decaying dipions to the total dipion production versus momentum transfer for each 100-MeV interval of dipion mass as tabulated in Tables VII and VIII. Data from 12 and 18 GeV/c have been combined statistically. The data were fit to $f(\theta) = a_0 + a_1 \cos\theta + a_2 \cos^2\theta$: $b_0 = a_0 + \frac{1}{3}a_2$; and $Q = a_0/b_0$.

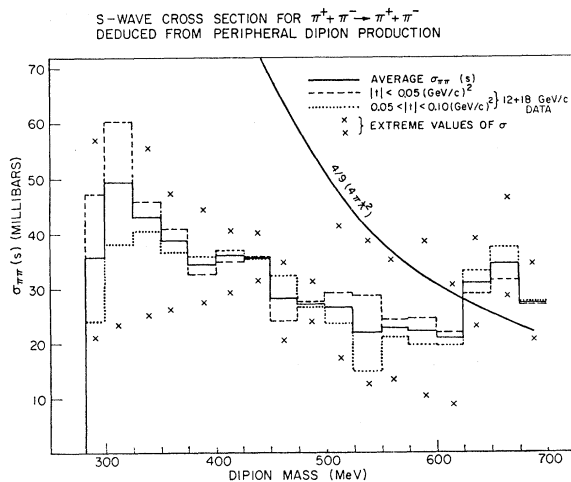


FIG. 27. The total cross section for the process $\pi^+\pi^- \rightarrow \pi^+\pi^-$ in the s -wave channel versus dipion mass as deduced from $\pi^- + N \rightarrow \pi^+ + \pi^- + (N + n\pi)$ for incident pions of 12 and 18 GeV/c and for two intervals of momentum transfer, $-t < 0.05$ (GeV/c) 2 and $0.05 < -t < 0.10$ (GeV/c) 2 . The solid histogram is the average of the four data subsets; dashed histograms represent the average over both incident pion momenta in each momentum transfer interval, and extreme values from the four data samples in each 25-MeV mass interval are indicated by 'x's. The unitarity limit for $J=T=0$ scattering, $(4/9)4\pi^2$, is also indicated.

$T=2$ phase shift is negligible,²² these cross sections can be used to find an s -wave phase shift and scattering length for the $J=T=0$ state. The results are given in Table XII and Fig. 27.

It is at first apparent that there are no resonances below 600 MeV which would approach saturation of the s -wave unitarity limit with a width of over several MeV.²³ In view of the good statistics at low dipion masses, these data are particularly significant on this point. The s -wave scattering length extrapolates to about 1.1 F at threshold. It is also apparent that there are no zeros in the s -wave pion-pion cross section or phase shift between threshold and 700 MeV.

These results could be in some error for several reasons. Near the ρ -meson region the isotropic com-

TABLE XI. The ratio Q of isotropic to total dipion production in 100-MeV dipion mass intervals. The weighted data were fit by $f(\theta) = a_0 + a_1 \cos\theta + a_2 \cos^2\theta$; $b_0 = a_0 + \frac{1}{3}a_2$; and $Q = a_0/b_0$.

Incident pion momentum (GeV/c)	Interval of dipion mass (MeV)	Intervals of four-momentum transfer $-t$ (GeV/c) 2		
		< 0.05	$0.05-0.10$	$0.10-0.20$
12	300-400	0.78 ± 0.16	0.62 ± 0.58	-0.58 ± 1.56
	400-500	1.03 ± 0.22	0.61 ± 0.28	1.19 ± 1.68
	500-600	0.73 ± 0.19	0.37 ± 0.16	1.19 ± 0.84
	600-700	1.00 ± 0.25	0.45 ± 0.16	0.30 ± 0.08
	700-800	0.35 ± 0.10	0.43 ± 0.11	0.15 ± 0.05
	800-900	0.12 ± 0.09	0.08 ± 0.05	0.37 ± 0.28
18	300-400	0.87 ± 0.17	0.57 ± 0.19	1.35 ± 0.56
	400-500	0.86 ± 0.24	0.57 ± 0.25	1.11 ± 1.26
	500-600	0.40 ± 0.19	0.70 ± 0.24	0.86 ± 0.55
	600-700	0.37 ± 0.16	0.48 ± 0.19	0.50 ± 0.20
	700-800	0.25 ± 0.11	0.40 ± 0.12	0.18 ± 0.08
	800-900		0.51 ± 0.25	0.38 ± 0.20
12 and 18 averaged	300-400	0.82 ± 0.12	0.58 ± 0.18	1.14 ± 0.52
	400-500	0.95 ± 0.16	0.59 ± 0.18	1.14 ± 1.01
	500-600	0.55 ± 0.13	0.47 ± 0.13	1.22 ± 0.52
	600-700	0.55 ± 0.13	0.46 ± 0.12	0.32 ± 0.08
	700-800	0.30 ± 0.08	0.42 ± 0.08	0.16 ± 0.04
	800-900	0.12 ± 0.09	0.10 ± 0.05	0.38 ± 0.17

ponent may come in part from depolarized ρ 's, and indeed this is probably the cause of the rise in the s -wave cross section above the unitarity limit near 650 MeV. Inelastic pion-nucleon scattering or production of other bosons (such as the ω) would contribute to the apparent s -wave pion-pion interaction cross section; however, these processes would generally produce apparent pions pairs with large momentum transfer and would depend on incident momentum. That the cross sections of Table XII do not seem to depend particularly on either

²² From $\pi^+p \rightarrow \pi^+\pi^+n$ and $\pi^-p \rightarrow \pi^-\pi^-N^{*++}$ bubble-chamber data, $\sigma_{\pi\pi}(T=2)$ falls from 14 mb threshold to 4 mb near the ρ mass corresponding to δ_0^2 rising from 5.5° to 20° in the same interval. See P. H. Satterblom, W. D. Walker, and A. R. Erwin, Phys. Rev. **134**, B207 (1964); Aachen-Berlin-Birmingham-Bonn-Hamburg-London (I.C.)-München Collaboration, *ibid.* **138**, B897 (1965); Saclay-Orsay-Bari-Bologna Collaboration, Nuovo Cimento **35**, 1 (1965).

²³ L. M. Brown and P. Singer, Phys. Rev. Letters **8**, 460 (1962); Phys. Rev. **133**, B812 (1964).

TABLE XII. The s -wave cross section for $\pi^+\pi^-\rightarrow\pi^+\pi^-$, phase shift, and scattering length as deduced from peripheral $\pi^-+N\rightarrow\pi^-\pi^++(N+n\pi)$ reactions.

Dipion mass m (MeV) \backslash ϕ	$\sigma_{\pi\pi}(s)$ in mb				Average $\sigma_{\pi\pi}(s)$	Phase ^a shift δ_0^0	Scattering length A_0^0 (F) ^{a,b}	Number of events
	$ t < 0.05$ (GeV/c) ²		$0.05 < t < 0.10$ (GeV/c) ²					
	12 GeV/c	18 GeV/c	12 GeV/c	18 GeV/c				
280	26.8	21.0	37.3	57.1	35.6			123
300	23.5	53.2	47.6	73.0	49.4	20°	1.12	262
325	25.0	55.7	39.4	52.2	43.1	25°	1.17	212
350	26.0	46.9	42.1	39.4	38.6	29°	1.23	173
375	27.4	44.3	30.5	34.4	34.2	32°	1.28	141
400	36.2	37.9	29.2	40.2	35.9	38°	1.51	136
425	36.1	34.6	31.4	40.0	35.6	43°	1.71	128
450	29.7	34.7	20.4	27.3	28.1	42°	1.57	97
475	25.5	27.5	23.7	31.1	27.0	44°	1.68	103
500	27.1	19.9	16.9	41.1	26.3	48°	1.89	109
525	12.5	17.1	18.8	38.5	21.8	47°	1.75	93
550	21.9	20.3	13.1	35.3	22.7	52°	2.10	95
575	27.2	11.9	10.2	38.5	22.0	55°	2.34	82
600	30.5	8.5	18.5	25.2	20.7	57°	2.44	88
625	39.0	26.9	23.0	34.4	30.9			98
650	46.5	28.2	28.5	34.5	34.5			119
675	34.4	20.4	24.6	28.9	27.1			92
700								
No. of events	799	510	473	369				Total No. of events=2151

^a Assuming $\delta_0^2=0$.^b $(A_0^0)^{-1} = k(k^2/\mu^2 + 1)^{-1/2} \cot \delta_0^0$.

incident momentum or momentum transfer seems encouraging evidence that what we see is genuine pion-pion scattering. It is also apparent from Table XI that the low-mass dipions are largely isotropic, whereas inelastic scattering would tend to give a predominantly forward negative pion, with correspondingly larger values of a_1 and a_2 than are seen. For this reason, it would be prudent, nevertheless, to regard our figures as upper limits to the s -wave pion-pion cross section. It is also not necessarily true that the s -wave production should be normalized to the ρ production in comparing the data and the calculations.

This normalization increases the cross section by always less than a factor of 2, as can be seen from Table IX, but it is subject to doubt for several reasons. While the same nucleon off-mass-shell terms pertain in both cases, the low-mass dipion production receives contributions from larger missing masses M' at a given momentum transfer than does the corresponding ρ production, as seen in Figs. 6 and 7. The entire ρ production data, but only the inelastic ρ production calculation, were compared for normalization; likewise the total s -wave data and only the inelastic s -wave calculation were used. The small error this introduces decreases with increasing dipion mass.²⁴ Also, effects due to absorption or to the presence of other nucleons in a target carbon nucleus may be different in the two cases, since the ρ emerges as a discrete single particle while the s -wave

²⁴ Note that in the lowest momentum transfer interval, the elastic ρ production is a 20% contribution to our data, but the larger range of M' permitted in this same t interval results in a much smaller elastic contribution to the data for $m < 450$ MeV (Fig. 28). As a result, our computed $\sigma_{\pi\pi}$ is probably low by about 20% for $-t < 0.05$ (GeV/c)² for the lowest dipion masses and by an amount which decreases as m increases toward the ρ mass. This trend may be seen in Table XII where the lower $|t|$ cross-section values are consistently low at low m .

scattered dipions at low mass emerge as two separate mesons. Again, however, the restriction to small momentum transfers [less than 0.1 (GeV/c)²] and lack of dependence of the cross section on t within this interval increase our confidence that our interpretation is substantially correct.

In Fig. 28 the missing-mass spectra for the 280–400-MeV regions of dipion mass are presented. No detailed calculations of the spectra were made.

D. Forward-Backward Asymmetry

The coefficient a_1 gives the amount of s -wave, p -wave mixing. A direct measure of this cross term in the angular distribution is a "polarization" P , where

$$P = (F - B) / (F + B);$$

F corresponds to $\theta < 90^\circ$, and B to $\theta \geq 90^\circ$. From the fitted coefficients we have also computed an equivalent P^* , where

$$P^* = a_1 / 2b_0.$$

If our data have no bias with $\cos\theta$, P and P^* would be equal. Using the raw data (unweighted numbers of events sorted into the appropriate bins), P is plotted in Fig. 29 for $-t < 0.10$ (GeV/c)² with the 12- and 18-GeV/c data taken together. The negative values of P below 500 MeV have not been observed in other experiments. This may be due to the better statistics here (well over 1000 events for m less than 500 MeV and low $-t$) and to the high energy of the experiment with the consequent reduction of background effects. It should be noted that inelastic pion scattering would contribute to positive values of a_1 and P . In order to explore the effect, the data below 450 MeV were combined as presented in Table XIII, where it is seen that

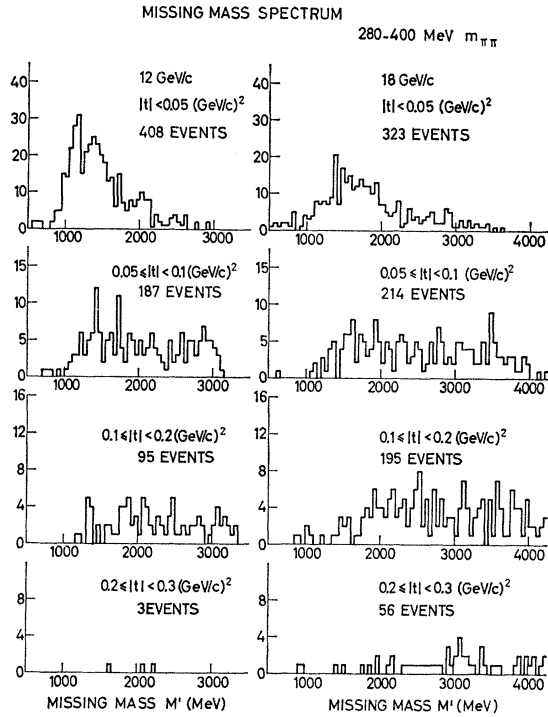


FIG. 28. The experimental distributions of missing mass M' for production of low-mass dipions ($m < 400$ MeV) for the different intervals of incident momentum and momentum transfer. The ordinates are numbers of events per 50 MeV.

P is negative in all intervals, and represents a $2\frac{1}{2}$ -standard-deviation effect over all. Extensive tests were made to see if the negative value of P was due to a bias in the geometry or the Čerenkov counter labeling. No such evidence was found; in fact, the small biases that may exist seem to favor slightly a positive value of P . It is certainly possible that the negative P value is a statistical fluctuation; the $2\frac{1}{2}$ -standard-deviation effect of Table XIII is less significant when it is noted that the cut in dipion mass was made after plotting Fig. 29.

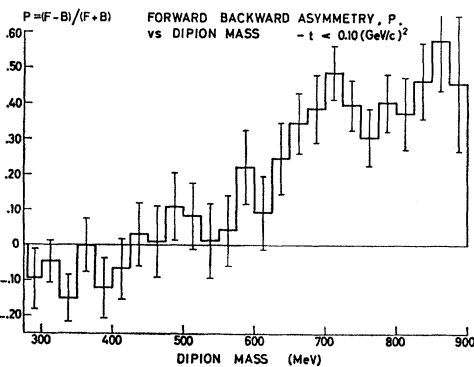


FIG. 29. The forward-backward asymmetry $P = (F - B)/(F + B)$ versus dipion mass for all data with $-t < 0.10$ (GeV/c)². F is the unweighted number of events where the π^- scattering angle in the dipion c.m. system, $\theta < 90^\circ$; and, correspondingly, B is the unweighted number of events where $\theta > 90^\circ$.

TABLE XIII. Forward-backward asymmetry P for dipions of mass below 450 MeV. $P = (F - B)/(F + B)$, where F is the number of events corresponding to a π^- scattering angle in the dipion c.m. system, $\theta < 90^\circ$, and B is the number for $\theta > 90^\circ$.

Incident pion momentum (GeV/c)	Upper limit of missing mass M' (MeV)	Range of four-momentum transfer $-t$ (GeV/c) ²	P (%)	Number of events
12	2500	< 0.05	-7.50 ± 4.60	467
		$0.05 - 0.10$	-3.96 ± 7.62	177
18	3000	< 0.05	-8.46 ± 5.38	343
		$0.05 - 0.10$	-3.71 ± 7.26	189
12 and 18	As above	< 0.10	-6.64 ± 2.91	1176

In Table XIV, values of P^* for each 100-MeV interval of dipion mass are given for the different cuts of momentum transfer. Again P^* is negative generally in the lowest mass cut, although for $0.05 < -t < 0.10$ (GeV/c)², P^* is positive where P is negative. This is an entirely reasonable consequence of the fitting process. The consequent errors confirm our reliance on P (from the raw data) rather than P^* (from the fits) for our interpretation. It is also consistent with the observation noted above that interpretations based on data subject to a minimum of manipulation are to be preferred.

Chew has suggested²⁵ that the s -wave $T=0$ phase shift may fall with increasing m , rather than rise. One consequence of this behavior would be a negative P for low m , although P would be positive again near the ρ resonance with $\delta_0^0 = -90^\circ$. As t increases, P tends to become more positive, as would be expected from a small contamination by inelastic π^- scattering. This suggests

TABLE XIV. The forward-backward asymmetry P^* in 100-MeV dipion mass intervals. The weighted data were fit by $f(\theta) = a_0 + a_1 \cos\theta + a_2 \cos^2\theta$; $b_0 = a_0 + \frac{1}{2}a_2$; and the asymmetry parameter $P^* = a_1/2b_0$.

Incident pion momentum (GeV/c)	Interval of dipion mass (MeV)	Intervals of four-momentum transfer $-t$ (GeV/c) ²		
		< 0.05	$0.05 - 0.10$	$0.10 - 0.20$
12	300-400	-0.16 ± 0.11	-0.13 ± 0.29	0.01 ± 0.31
	400-500	0.03 ± 0.12	-0.18 ± 0.15	-0.02 ± 0.08
	500-600	0.25 ± 0.16	0.15 ± 0.16	0.03 ± 0.10
	600-700	-0.13 ± 0.30	0.32 ± 0.14	0.44 ± 0.13
	700-800	0.43 ± 0.14	0.37 ± 0.14	0.23 ± 0.10
	800-900	0.39 ± 0.28	0.21 ± 0.15	0.17 ± 0.31
18	300-400	-0.06 ± 0.21	0.15 ± 0.17	-0.09 ± 0.09
	400-500	0.12 ± 0.18	0.15 ± 0.22	0.20 ± 0.20
	500-600	0.22 ± 0.19	0.20 ± 0.19	0.01 ± 0.20
	600-700	0.44 ± 0.20	-0.01 ± 0.19	0.50 ± 0.18
	700-800	0.49 ± 0.19	0.39 ± 0.16	0.25 ± 0.11
	800-900		0.05 ± 0.28	0.29 ± 2.15
12 and 18 averaged	300-400	-0.12 ± 0.09	0.08 ± 0.15	-0.08 ± 0.09
	400-500	0.02 ± 0.10	-0.07 ± 0.13	0.01 ± 0.07
	500-600	0.24 ± 0.12	0.17 ± 0.12	0.02 ± 0.09
	600-700	0.26 ± 0.17	0.21 ± 0.12	0.46 ± 0.10
	700-800	0.45 ± 0.11	0.38 ± 0.10	0.24 ± 0.07
	800-900	0.39 ± 0.28	0.20 ± 0.15	0.17 ± 0.31

²⁵ G. F. Chew, Phys. Rev. Letters 16, 60 (1966).

that even the lowest $|t|$ cut may underestimate this effect, and that the mass at which P passes through zero is probably higher than the value given here. It is also plausible that this background could completely mask the effect in previous low-energy experiments. If P is negative, it would be due to a negative value either of δ_0^0 or of δ_1^1 ; however, at least at the ρ^0 mass, δ_1^1 is known to be positive.²⁶ The δ_0^2 phase shift is known from bubble-chamber data to be small and negative.²² If δ_0^0 is negative at low m , the δ_0^2 amplitude would add constructively to that from δ_0^0 in the reaction $\pi^+\pi^- \rightarrow \pi^+\pi^-$, while they would add destructively in $\pi^+\pi^- \rightarrow \pi^0\pi^0$. This is in qualitative agreement with a comparison between the present data and unpublished $\pi^0\pi^0$ data from the Oxford group.^{27,28}

Plots of P^* versus t in each mass interval averaged over the 12- and 18-GeV/ c data are included in Fig. 30. Regrettably, the statistics do not permit clear conclusions in each mass interval, so that only the ρ case discussed below and the predominantly negative P^* for low m warrant discussion. However, these tables and graphs may serve to point out how improved data over the entire mass range could be used to determine the physical pion-pion interaction through extrapolation to the pole, in the manner originally urged by Chew and Low.²⁹ In order to explore the extent to which δ_0^0 is resonant in the energy region $700 < m < 800$ MeV, the values of P^* from Table XIV have been studied in this mass interval in particular. As noted for the low-mass data, background effects would generally modify P with increasing $-t$ and off-mass-shell terms would reduce the ratio δ_0^0/δ_1^1 . The values of P^* plotted in Fig. 30 were extrapolated to $t = \mu^2$. From Eq. (3a), $P^* = 0.58$ for $\delta_0^0 = \delta_1^1$; $\delta_0^2 = 0$. Experimentally, $P^* = +0.525$ at the pole corresponding to $\sin\delta_0^0 = \pm 0.92$ for $\delta_1^1 = 90^\circ$, $\delta_0^2 = 0$. (The value of δ_0^2 is known to be about -20° in this mass range.²²) These data are then consistent with δ_0^0 close to $\pm 90^\circ$, and the lower-energy data suggest that $|\sin\delta_0^0|$ is growing slowly toward unity.

VIII. SUMMARY

A very-high-momentum experiment has been used to study the peripheral process and pion-pion interactions.

²⁶ C. Lovelace has pointed out that one possible source of a zero in δ^1 could be the interpretation of the ρ meson as a Castellejo-Dalitz-Dyson pole (private communication).

²⁷ I. F. Corbett, C. J. S. Damerell, N. Middlemas, D. Newton, A. B. Clegg, and W. S. C. Williams, Phys. Rev. **156**, 1451 (1967); and A. B. Clegg (private communication).

²⁸ The existing K_{e4} data suggest a positive δ_0^0 near threshold [R. W. Birge *et al.*, Phys. Rev. **139**, B1600 (1965) and C. T. Murphy, in *High Energy and Particle Physics*, edited by W. E. Brittin, A. O. Barut, and M. Guenin (Gordon and Breach Science Publishers, Inc., New York, 1967), Vol. IX B, p. 171]. Recently L. D. Jacobs and W. Selove [Phys. Rev. Letters **16**, 669 (1966)] have analyzed $\pi^-\pi^+$ production in bubble-chamber data and have also concluded that δ_0^0 is positive, although the conclusions are based on an order of magnitude fewer events, larger momentum transfers, and lower energies than this study.

²⁹ G. F. Chew and F. E. Low, Phys. Rev. **113**, 1640 (1959).

DIPION FORWARD-BACKWARD ASSYMMETRY, P^* , VS MOMENTUM TRANSFER, t , FOR DIFFERENT DIPION MASS INTERVALS

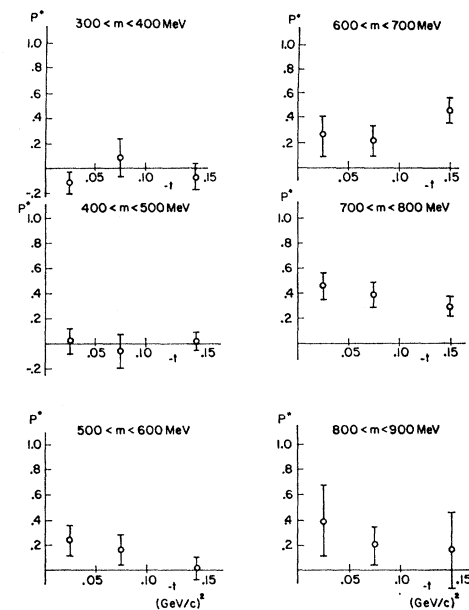


Fig. 30. The forward-backward asymmetry P^* as deduced from $\cos\theta$ expansions of the weighted data versus four-momentum transfer in 100-MeV intervals of dipion mass taken from Table XIV. Data from 12 and 18 GeV/ c have been combined statistically. The data were fit to $f(\theta) = a_0 + a_1 \cos\theta + a_2 \cos^2\theta$; $b_0 = a_0 + \frac{1}{3}a_2$; and $P^* = a_1/2b_0$.

The one-pion-exchange process qualitatively explains the ρ^0 production data. The missing-mass spectra accompanying the ρ production corroborate this model, and the point is noted that inelastic channels at the nucleon vertex may account for some of the cross section which, in elastic ρ production, is attenuated by absorption processes. It is further observed that the inelastic cross section as calculated is almost independent of incident momentum and momentum transfer at high energies. A detailed study of the s -wave dipion interaction is carried out using the rich low-dipion-mass data herein. A monotonically falling $\pi\pi$ s -wave cross section is deduced, corresponding to a slowly varying phase shift which may pass near $\pm 90^\circ$ close to the ρ mass. The cross-section data together with the observed negative forward-backward asymmetry for low dipion mass are consistent with a negative $J=T=0$ phase shift falling smoothly from threshold. Moreover, we see no evidence of a relatively narrow ϵ^0 resonance.

More generally, we have learned that an approach to the analysis can be successfully exploited in which an integration over final states at one of two peripheral vertices permits detailed study of the other vertex. As detailed experiments are pressed to higher and higher energies, where cross sections for each particular channel continue to fall, the methods of this experiment may find broad application.

ACKNOWLEDGMENTS

We would like to acknowledge the indispensable assistance in this experiment of W. Beck, H. Kuhn, L. Griffith, and C. Symons of CERN, and of E. Coleman, B. Loo, and S. Powell of The University of Michigan. A major part of the analysis was carried out at The University of Michigan including film measurement and digital calculation, and was supported by the U. S. Office of Naval Research Contract No. Nonr

1224(23). Film measurements at M.I.T. were supported by the U. S. Atomic Energy Commission. Valuable assistance in film prescanning was carried out at the University of Bologna under the direction of G. Giacomelli. We have benefited significantly from discussions on the theoretical interpretations of these data with G. Chew, R. Deck, S. Drell, C. Lovelace, and B. Svensson. Finally, it is a pleasure to express our gratitude to CERN for its hospitality during the course of this experiment and the subsequent analysis.

Four- and Five-Body Final States from 3-GeV/ c π^-p Interactions*

A. W. KEY, J. D. PRENTICE, N. R. STEENBERG, E. WEST, AND T. S. YOON
University of Toronto, Toronto, Canada

AND

W. A. COOPER, W. MANNER, AND L. VOJVODIC
Argonne National Laboratory, Argonne, Illinois

AND

W. D. WALKER
University of Wisconsin, Madison, Wisconsin

(Received 25 August 1967)

Approximately 3600 four-prong events produced by π^-p interactions at 2.96 GeV/ c have been analyzed. The $p\pi^+\pi^-\pi^-$ channel shows production of $N^{*++}(1238)$ [(41±4)%], ρ^0 [(40±5)%], and A_2^- [(7±2)%]. Some evidence for associated $N^{*0}\rho^0$ production is also observed. The one-pion-exchange mode with form factor is shown to give an adequate description of the $N^{*0}\rho^0$ events. The $N^{*++}\pi^-\pi^-$ events are analyzed within the framework of this model, and the $I=2$ $\pi\pi$ scattering cross section up to $m(\pi\pi)\simeq 1$ GeV/ c^2 is calculated. A value for the $I=2$ $\pi\pi$ s -wave scattering length of $|a_2^0|=0.19m_\pi^{-1}$ is obtained. In a determination of the spin and parity of the A_2 meson, the 2^+ assignment is favored throughout the fairly wide range of experimental uncertainties in the estimate of the background in the A_2 region. The $p\pi^+\pi^-\pi^0$ channel is dominated by production of ω^0 [(26±2)%] and $N^{*++}(1238)$ [(30±6)%]. ρ^- , ρ^0 , and $N^{*+}(1238)$ are produced much more weakly. Peripheralities are much less pronounced than in the four-constraint fits. No B meson is observed in the present data. The observation of enhancements at 2080 and 2190 MeV/ c^2 in the $p\pi^+\pi^-\pi^0$ spectrum has been reported previously. The $n\pi^+\pi^+\pi^-\pi^-$ channel shows strong $N^{*-}(1238)$ production [(50±10)%] and some weak ρ^0 production.

I. INTRODUCTION

THIS paper presents an analysis of four-prong events produced by π^- mesons of 2.96 GeV/ c in hydrogen. The two-prong events have been reported previously.¹ The events have been classified as

$$\begin{aligned}\pi^-p &\rightarrow p\pi^+\pi^-\pi^-, & 1608 \text{ events (1)} \\ &\rightarrow p\pi^+\pi^-\pi^-\pi^0, & 1412 \text{ events (2)} \\ &\rightarrow \pi^+\pi^+\pi^-\pi^-n. & 620 \text{ events (3)}\end{aligned}$$

Resonance production is observed in all these final states, but, in particular, reaction (1) is used to study $\pi\pi$ scattering in the $I=2$ channel and the decay of the

A_2 meson; reaction (2) has indicated the production of a new N^* of mass 2080 MeV/ c^2 ; and reaction (3) shows some anomalies in the production of known isobars. These topics are discussed in this order in the sections that follow. Many similar experiments have been carried out for pions up to about 4 GeV/ c . References 2 and 3 contain full bibliographies.

The events were taken from an exposure of 50 000 pictures in the 30-in. ANL-MURA hydrogen bubble chamber at the Argonne ZGS. Seventy millimeter film and a high field (32 kG) allowed accurate measurements to be made using conventional film plane and image

* Work supported in part by the U. S. Atomic Energy Commission and the National Research Council of Canada.

¹ D. R. Clear, T. F. Johnston, J. Pilcher, J. D. Prentice, N. R. Steenberg, E. West, T. S. Yoon, W. A. Cooper, W. Manner, L. Vojvodic, and W. D. Walker, *Nuovo Cimento* **49A**, 399 (1967).

² Suh Urk Chung, Ph.D. thesis, University of California Radiation Laboratory UCRL Report No. 16881, 1966 (unpublished).

³ P. R. Klein, R. J. Sahni, A. Z. Kovacs, and G. W. Tautfest, *Phys. Rev.* **150**, 1123 (1966) Aachen-Berlin-Birmingham-Bonn-Hamburg-London (I.C.)-München Collaboration, *Nuovo Cimento* **31**, 485 (1964).

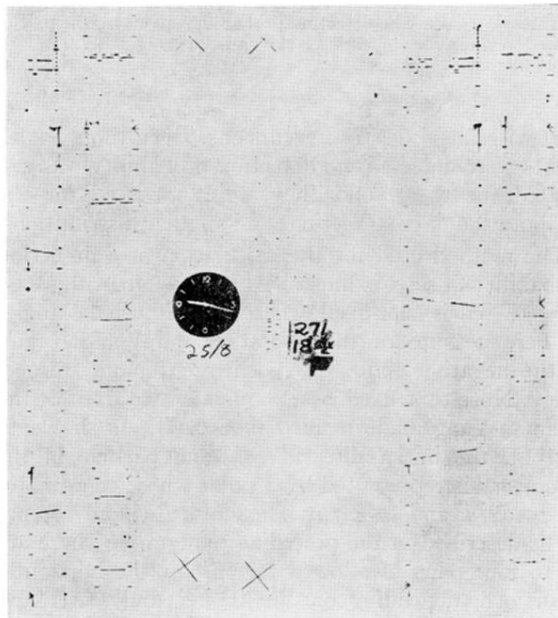


FIG. 12. A film frame of a typical dipion event. The spark chambers are bordered by fiducial lights.